



저작자표시-비영리-변경금지 2.0 대한민국

이용자는 아래의 조건을 따르는 경우에 한하여 자유롭게

- 이 저작물을 복제, 배포, 전송, 전시, 공연 및 방송할 수 있습니다.

다음과 같은 조건을 따라야 합니다:



저작자표시. 귀하는 원 저작자를 표시하여야 합니다.



비영리. 귀하는 이 저작물을 영리 목적으로 이용할 수 없습니다.



변경금지. 귀하는 이 저작물을 개작, 변형 또는 가공할 수 없습니다.

- 귀하는, 이 저작물의 재이용이나 배포의 경우, 이 저작물에 적용된 이용허락조건을 명확하게 나타내어야 합니다.
- 저작권자로부터 별도의 허가를 받으면 이러한 조건들은 적용되지 않습니다.

저작권법에 따른 이용자의 권리와 책임은 위의 내용에 의하여 영향을 받지 않습니다.

이것은 [이용허락규약\(Legal Code\)](#)을 이해하기 쉽게 요약한 것입니다.

[Disclaimer](#)



공학석사학위논문

Carboxyl-functionalized Metal-Organic Frameworks for Adsorptive Removal of Toxic Chemicals in Oily Phase

카르복실기가 표면에 개질된 금속-유기 골격체를 이용한
유증 유해물질 흡착 제거에 대한 연구

2020년 2월

서울대학교 대학원
재료공학부
최성규

Abstract

Carboxyl-functionalized Metal-Organic Frameworks for Adsorptive Removal of Toxic Chemicals in Oily Phase

Sunggyu Choi

Department of Materials Science and Engineering

The Graduate School

Seoul National University

This study aims to apply and optimize the adsorption process for toxic chemicals, such as quinoline, 3-MCPD and glycidol, in oily phase using carboxyl-functionalized Metal-Organic Frameworks (MOFs). In order to analyze the adsorption performance, three MOFs were synthesized with different ligands to control of the structure of the MOF. Among the samples, Fe-MIL-88_BDC synthesized with terephthalic acid showed the highest specific surface area. The high surface area resulted in efficient adsorption performance because open metal sites could be easily exposed. For all toxic

chemicals, Fe-MIL-88_BDC exhibited superior adsorption performance. In terms of adsorption kinetics, Fe-MIL-88_BDC showed the fastest adsorption rate.

To further improve the adsorption performance of Fe-MIL-88_BDC, the ligands were functionalized with carboxyl groups. Ligand functionalization reduced pore contraction, improving the pore volume and surface area of Fe-MIL-88_BDC-COOH. The maximum adsorption performance and initial adsorption rate of toxic chemicals were improved by the increment of surface area by providing additional acid-base interaction and carboxyl group which can form covalent bond with functionalized ligand. This study shows the possibility of adsorption and removal of toxic chemicals in oily phase by using MOFs and provides systematic data on the synthesis and selection of MOFs applied in oily phase.

Keywords

Metal-organic framework, Adsorption, Oily phase, Toxic chemicals, Carboxyl-functionalization, Kinetics, Isotherms

Student number: 2018-27551

Contents

1. Introduction.....	1
2. Experimental.....	8
2.1. Materials	8
2.2. Synthesis of Fe-MIL-88s using various ligands.....	8
2.2.1 Synthesis of Fe-MIL-88_NDC	8
2.2.2 Synthesis of Fe-MIL-88_BDC	9
2.2.3 Synthesis of Fe-MIL-88_BPDC	10
2.3. Synthesis of carboxyl-functionalization of Fe-MIL-88_BCD	12
2.4. Characterization	14
2.4.1 Crystal structure	14
2.4.2 Morphology.....	14
2.4.3 Pore textural property	15
2.4.4 Chemical structure.....	15
2.4.5 Thermal behavior.....	15
2.5. Adsorption test for toxic chemicals	16
2.5.1 Calibration curve of standard solution.....	16
2.5.2 Adsorption kinetics	17
2.5.3 Adsorption isotherms	19
3. Results and discussion.....	24

3.1. Characteristics of the synthesized Fe-MIL-88s.....	24
3.1.1 Structural property	24
3.1.2 Morphology	31
3.1.3 Chemical structure	34
3.1.4 Thermal behavior.....	36
3.2. Evaluation of adsorption performance of various Fe-MIL-88s toward toxic chemicals	38
3.2.1 Adsorption kinetics	38
3.2.2 Adsorption isotherms	45
3.3. Characteristics of the carboxyl-functionalized Fe-MIL-88_BCD .	52
3.3.1. Structural property	52
3.3.2. Morphology	57
3.3.3. Chemical structure.....	59
3.3.4. Thermal behavior.....	61
3.4. Evaluation of adsorption performance of carboxyl-functionalized Fe-MIL-88_BCD	63
3.4.1. Adsorption kinetics	63
3.4.2. Adsorption isotherms	69
4. Conclusion	81
5. References.....	83
6. Korean ABSTRACT.....	92

1. Introduction

As an engineered process, adsorption technology has many applications ranging from treatment of various pollutants to separation and removal of specific chemicals for both liquid and gas phases due to simple and cost effective process [1]. Besides, adsorption technology is particular interest for oil processing, as the oil contains numerous organic compounds [2]. With increasing world's population and improving standard of living, the world's demand for various oils such as fuels and edible oils is substantially increasing [3-5]. However, Toxic chemicals such as quinoline, 3-MCPD esters and glycidyl esters in oily phase have a negative impact on the environment and human body. Quinoline is one of the various nitrogen containing compounds in fuel and has toxic and carcinogenic activity to the humans (**Figure 1**) [6, 7]. In addition, quinoline produces nitrogen oxides upon combustion, which act as a major cause of smog and acid rain, thus adversely affecting the environment [8, 9]. Quinoline also reduces the activity and lifetime of catalysts that remove sulfur-containing compounds in fossil fuels [10]. 3-chloropropane-1,2-diol (3-MCPD) esters and glycidyl esters are produced under high temperature conditions of deodorization during the refining of edible oils [11, 12]. When ingested refined oil, these materials might undergo hydrolysis and converted to 3-MCPD and glycidol

in the human body [13].

Many researchers and manufacturers have suggested various methods for removing toxic chemicals such as nitrogen-containing compounds, 3-MCPD and glycidol [14]. Hydrotreating requires high temperature and pressure. In addition, a large amount of hydrogen should be used and is inefficient in price [15]. The ion-exchange method has some disadvantages such as needs for chemicals to regenerate, high installation cost, and limited use at high temperature [16]. Oxidation methods proceed in multistep and the appropriate solvent should be used in the extraction step. Corrosive oxidizing agents are used in the extraction stage and energy consumption is high [17]. Since the various methods previously used have several limitations, adsorption is drawing attention to remedy these limitations [18]. Various organic and inorganic materials have been applied to adsorption. These include mesoporous silica, zeolite, graphene oxide and activated carbon, etc. However, mesoporous silica and zeolite are not well dispersed in oil. The functionality is also limited. Carbon-based materials also have disadvantages such as low selectivity and limited functionality [14, 19].

Although several materials are being applied for adsorptive removal for various toxic chemicals in oily phase, Metal-Organic Frameworks (MOFs) are the most promising and recently established adsorbents that can be effectively applied for adsorption in oily phase because of facile structural

control and functionalities [20]. MOFs are porous materials made from metal-containing nodes and organic linkers. Typical characteristics of MOF are high chemical and thermal stability, ultrahigh porosity, and structural diversity. Due to these characteristics, it is applied to various fields such as gas storage [21], separation [21], catalysis and chemical sensing [22] (**Figure 2**). These properties can also have a favorable effect on adsorption in the liquid phase [23].

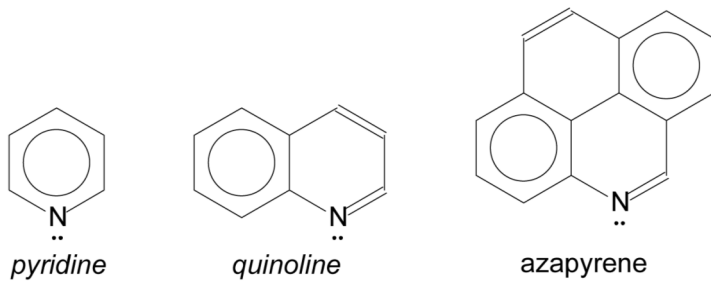
The main mechanisms for adsorption of MOF are acid-base interaction, covalent bond and van der waals force [14]. Acid-base interaction is common and easily understood mechanism of MOF. Acid-base interaction with adsorbates occurs through open metal sites such as Fe^{3+} , Cr^{3+} and V^{3+} or surface functionalization [24]. Van der waals force is applicable at ambient temperatures, and since the adsorption process usually proceeds at low or ambient temperatures, van der waals force can be easily applied in adsorption [25]. Covalent bond can be achieved by functionalization of MOFs. It mainly forms covalent bonds with adsorbates by adding functional groups to the ligand [26].

Various MOFs have been studied for adsorption in the liquid phase, especially in the oily phase due to high adsorption capacity. Among them, Fe based MIL-88 has several notable features. Fe-MIL-88 series are cheap, biocompatible and biodegradable. Furthermore, These MOFs have high

chemical and thermal stability [27]. The structure of Fe-MIL-88 consists of the trimers of iron(III) and the dicarboxylate groups such as terephthalic acid, 2,6-naphthalenedicarboxylic acid and 4,4'-biphenyldicarboxylic acid. Regardless of ligand types, each material exhibits the same symmetry and space group [28] (**Figure 3 and 4**). However, there is no application of Fe-MIL-88 series in oily phase. So, it is necessary to study how adsorption performance of Fe-MIL-88 series changes depending on the type of ligands.

In this study, we prepared various Fe-based MIL-88s using a hydrothermal reaction. The properties of the synthesized Fe-MIL-88s are characterized with crystal structure, surface area, surface chemistry and morphology. The synthesized Fe-MIL-88s are used to adsorb quinoline, 3-MCPD and glycidol. After adsorption, the residual quinoline concentration is analyzed by a UV-vis spectroscopy and 3-MCPD and glycidol are analyzed by a ^1H nuclear magnetic resonance (^1H NMR) spectroscopy. The adsorption kinetics are fitted to the pseudo-first order (PFO) and pseudo-second order (PSO) equation. To confirm the maximum adsorption capacity and adsorption mechanism, the adsorption isotherms are fitted to the Freundlich and Langmuir model. After carboxyl-functionalization of the best superior adsorbents, the adsorption performance was analyzed and compared.

Pyridines (basic nitrogen)



Pyrroles (non-basic nitrogen)

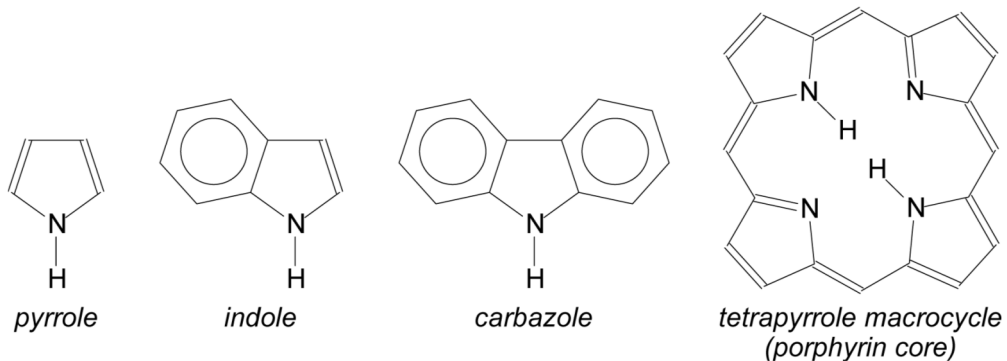


Figure 1. Examples of various nitrogen-containing compounds [6]

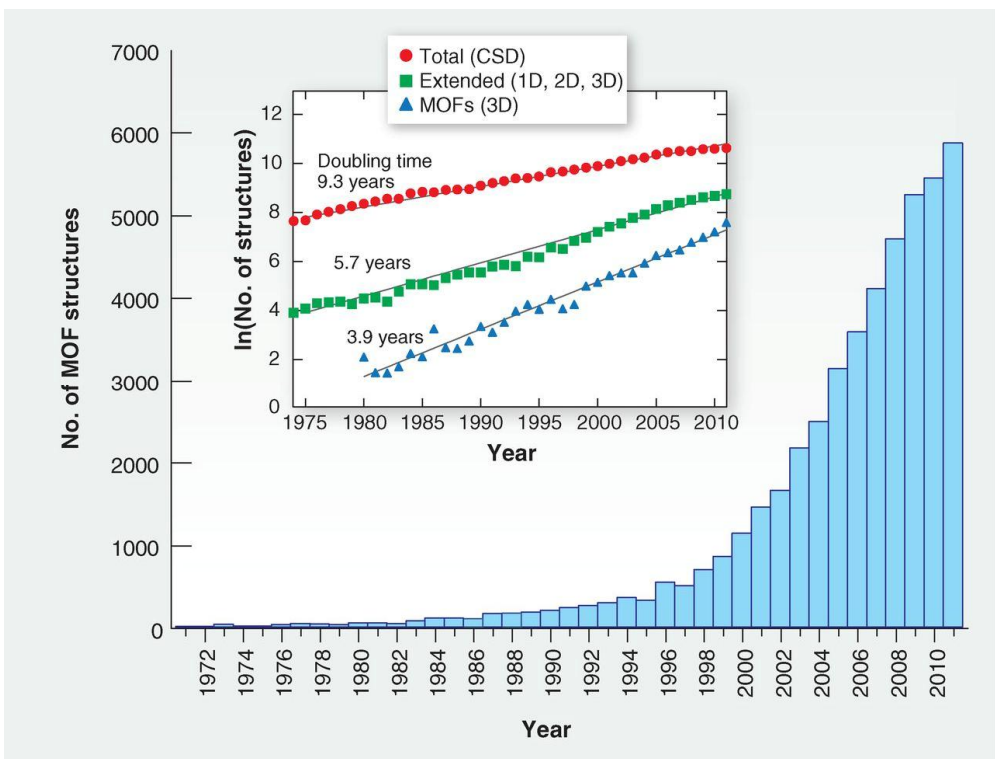


Figure 2. Number of Metal-Organic frameworks structures [20]

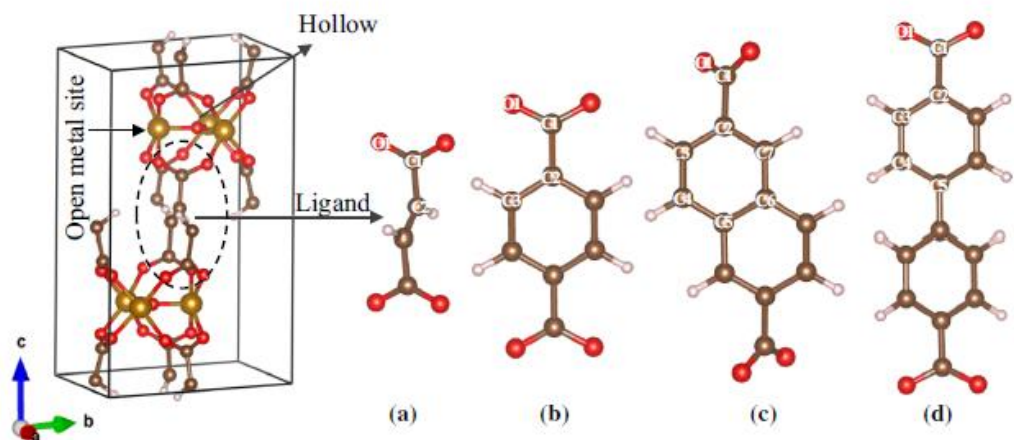


Figure 3. Structure of Fe-MIL-88s with different ligands [27]

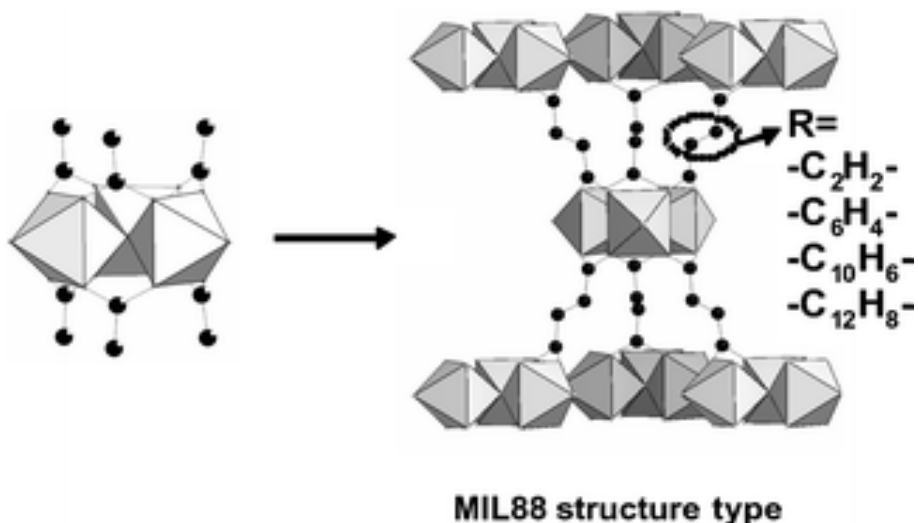


Figure 4. Structure of Fe-MIL-88s for (001) plane [29]

2. Experimental

2.1. Materials

Iron(III) chloride hexahydrate (98%, Daejung) was used as a metal ion cluster. Terephthalic acid (98%, Sigma-Aldrich), 2,6-naphthalenedicarboxylic acid (95%, Sigma-Aldrich), Biphenyl-4,4'-dicarboxylic acid (97%, Sigma-Aldrich), 2-Aminoterephthalic acid (99%, Alfa Aesar) were used for synthesizing various Fe-MIL-88s. Maleic anhydride ($\geq 99.0\%$, Sigma-Aldrich) was used for carboxyl-functionalization. N,N-Dimethylformamide (99.5%, Daejung, Korea), n-Octane (95%, Samchun, Korea), Toluene (99.5%, Daejung, Korea), Isopropyl alcohol (99.5%, Daejung, Korea), Dichloromethane (99.5%, Daejung, Korea) were used as an organic solvent. Quinoline (97%, Alfa Aesar), (\pm)-3-Chloro-1,2-propanediol (98%, Sigma-Aldrich), (\pm)-Glycidol (96%, Sigma-Aldrich) were used as a adsorbate. Chloroform-d (99.8 atom %D, Sigma-Aldrich) was used as a NMR solvent.

2.2. Synthesis of Fe-MIL-88s using various ligands

2.2.1 Synthesis of Fe-MIL-88_NDC

Synthesis of Fe-MIL-88_NDC was conducted according to a previously reported method. Firstly, 2.56 g of Iron(III) chloride hexahydrate and 2.08 g of 2,6-naphthalenedicarboxylic acid were put into 250 ml 3-neck round-bottomed flask and 100 ml of DMF was added. Secondly, the solution was reacted with reflux at 130 °C under continuous stirring for 18 h. The product was filtered and washed several times with DMF and ethanol and dried under vacuum condition at 80 °C for 24 h [30]. Overall scheme is subscribed in **Figure 5 and Table 1.**

2.2.2 Synthesis of Fe-MIL-88_BDC

Synthesis of Fe-MIL-88_BDC was conducted according to a previously reported method. Firstly, 1.35 g of Iron(III) chloride hexahydrate was dissolved in 45 ml of DMF at room temperature under stirring for 20 min, named solution A. Using another vial, 0.83 g of Terephthalic acid was dissolved in 45 ml of DMF at room temperature under stirring for 15 min, named solution B. Secondly, solution B was added to the solution A. Then, mixed solution was stirred at room temperature for 30 min to achieve a

homogeneous solution. The mixed solution was transferred into a Teflon-lined autoclave and placed in an oven at 110 °C for 24 h. The product was filtered and washed several times with DMF and ethanol and dried under vacuum condition at 80 °C for 24 h [31]. Overall scheme is subscribed in **Figure 5 and Table 1**.

2.2.3. Synthesis of Fe-MIL-88_BPDC

Synthesis of Fe-MIL-88_BPDC was conducted according to a previously reported method. Firstly, 1.62 g of Iron(III) chloride hexahydrate and 0.84g of Biphenyl-4,4'-dicarboxylic acid were dispersed in 30 ml of DMF. The dispersed solution was transferred into a Teflon-lined autoclave and placed in an oven at 100 °C for 12 h. The product was filtered and washed several times with DMF and ethanol and dried under vacuum condition at 80 °C for 24 h [32]. Overall scheme is subscribed in **Figure 5 and Table 1**.

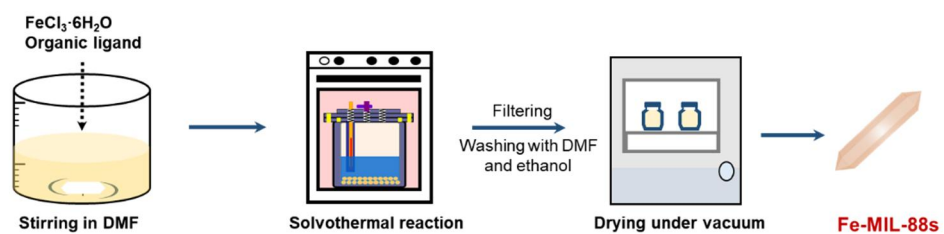


Figure 5. Schematic illustration of synthesis of Fe-MIL-88s using various organic ligands

Fe-MIL-88_NDC	FeCl ₃ ·6H ₂ O (2.56 g)	2,6-Naphthalen dicarboxylic acid (2.08 g)
Fe-MIL-88_BDC	FeCl ₃ ·6H ₂ O (1.35 g)	Terephthalic acid (0.84 g)
Fe-MIL-88_BPDC	FeCl ₃ ·6H ₂ O (1.62 g)	4,4'-biphenyl dicarboxylic acid (0.84 g)

Table 1. Synthetic condition of Fe-MIL-88 series

Fe-MIL-88_NDC	DMF 100 ml	130 °C, 18 h
Fe-MIL-88_BDC	DMF 45 ml	100 °C, 24 h
Fe-MIL-88_BPDC	DMF 30 ml	100 °C, 12 h

2.3. Synthesis of carboxyl-functionalization of Fe-MIL-88_BDC

Synthesis of amine-functionalization Fe-MIL-88_BDC was conducted according to a previously reported method. 1.13 g of Iron(III) chloride hexahydrate, 1.89g of 2-Aminoterephthalic acid and 0.75 g of distilled water were dispersed in 70 ml of DMF. Subsequently, the dispersed solution was transferred into a Teflon-lined autoclave and placed in an oven at 150 °C for 3 days. The product was filtered and washed several times with copious DMF and ethanol and dried under vacuum condition at 80 °C for 24 h [33]. Secondly, 600 mg of the synthesized powder, named Fe-MIL-88_BDC-NH₂ and 600 mg of maleic anhydride were mixed in 30 ml of dichloromethane at

room temperature for 2 days. The final powders were filtered and washed with dichloromethane and ethanol and dried under vacuum condition at 80 °C for 24 h [34]. Overall scheme is subscribed in **Figure 6**.



Figure 6. Schematic illustration of synthesis of carboxyl-functionalized Fe-MIL-88_BDC-COOH

2.4. Characterization of synthesized Fe-MIL-88s

2.4.1 Crystal structure

X-ray diffraction (XRD) measurements were applied to identify the crystallinity of the synthesized Fe-MIL-88s. using Bruker New D8-Advance with CuK α radiation ($\lambda = 1.5406 \text{ \AA}$) generated at a voltage of 40 kV and a current of 40 mA. The scattering angle ranges between 5 to 40° at 2°min^{-1} . The crystallite sizes were obtained by using the Scherrer equation ($\Phi = K\lambda/\beta\cos\theta$), where Φ is the crystallite size, λ is 0.154 nm that is the wavelength of the X-ray irradiation, K is usually assumed taken as 0.89, β is the full width at half-maximum intensity (FWHM), and θ is bragg angle for various Fe-MIL-88s. Bragg's law ($n\lambda = 2d\sin\theta$) was used to determine the spacing between layers for different types of ligands. In the equation of bragg's law, d is the spacing between layers.

2.4.2 Morphology

Surface morphologies of the synthesized Fe-MIL-88s was observed with field-emission scanning electron microscopy (FE-SEM, SIGMA, applied voltage: 3.0 kV) with surface platinum coating. To analyze each particle's

size and morphology, high resolution-transmission electron microscopy (HR-TEM, JEOL JEM-3010) was performed.

2.4.3. Pore textural property

Nitrogen adsorption-desorption isotherms were measured with a Micrometrics ASAP 2020 apparatus after all the samples were degassed at 150 °C for 6 h. The specific surface area of the synthesized Fe-MIL-88s was estimated by utilizing the Brunauer-Emmett-Teller (BET) method. Pore volume and pore size distributions were calculated by the Barrett-Joyner-Halenda (BJH) method.

2.4.4. Chemical structure

Fourier-transform infrared (FT-IR) spectroscopy characterization of the synthesized Fe-MIL-88s for monitoring of the modification was performed using Thermo Scientific Nicolet spectrophotometer with a spectral resolution of 4 cm^{-1} in the range of 500 – 4000 cm^{-1} . All synthesized samples were prepared by compression-molding and potassium bromide (KBr) powder was used as sample matrix and reference material.

2.4.5. Thermal behavior

Thermal behavior of various Fe-MIL-88s were analyzed by

thermogravimetric analysis (TGA). Thermogravimetric analysis was carried out using SDT Q-600 under flowing oxygen. Temperature ranges were from room temperature to 500 °C and heating rate was 10 °C/min. The masses of the samples were approximately 5 ~ 10 mg. Thermal degradation stability of the synthesized Fe-MIL-88s were calculated using the temperature of 10 % weight loss of the samples, T_{d10} .

2.5. Adsorption test for toxic chemicals

2.5.1. Calibration curve of standard solution

For the calibration of quinoline, n-octane was used to make solutions with concentrations of 50, 25, 12.5, 6.25 and 3.125 ppm, respectively. The concentrations of quinoline were determined by using UV-Vis spectroscopy (Lambda 25 UV-Vis Spectrometer). The UV absorbance at 313 nm was to calculate the concentrations of quinoline [8].

For the calibration of 3-MCPD and glycidol, isopropyl alcohol and toluene were thoroughly mixed to make a standard solution. The ratio of isopropyl alcohol and toluene was set to 1:1 (w/w) at room temperature. To make a solution with concentrations of 2, 4, 6, 8 and 10 wt%, 3-MCPD and glycidol were added to the co-solvent. Proton nuclear magnetic resonance (^1H NMR, Bruker AVANCE 600) spectroscopy was been used to determine the

concentrations of standard solutions by calculating the peaks of integration.

2.5.2. Adsorption kinetics

All adsorption kinetic experiments were carried out by a batch method. The adsorption kinetic experiments were divided according to the type of media in which toxic chemicals exist. For the adsorption kinetics of quinoline, stock solutions of quinoline with a concentration with 50 ppm were prepared by dissolving a proper amount of quinoline in n-octane. The experiments for evaluating adsorption kinetics were conducted at room temperature with different times (5, 15, 30, 60, 120 and 720 min) in the 50 ml propylene conical tubes by adding 5 mg of synthesized Fe-MIL-88s into the 20 ml of quinoline solution. When the adsorption kinetics experiments were finished, the particles were filtered with hydrophobic syringe filter (Advantec, average pore size: 0.1 μm). The filtered solution was analyzed with a UV-vis spectroscopy. The UV absorbance at 313 nm was to calculate the concentrations of quinoline.

For adsorption kinetics of 3-MCPD and glycidol, Exact amounts of 3-MCPD and glycidol were dissolved in co-solvent of isopropyl alcohol and toluene to make a concentration of 10 wt%. The adsorption tests for adsorption kinetics were conducted at room temperature with different times (5, 15, 30, 60, 120 and 720 min) in 10 ml glass vial by adding 50 mg of Fe-

MIL-88s into the 1 g of 3-MCPD and glycidol solution (1:20 w/w). When the adsorption kinetics experiments were finished, the particles were filtered with hydrophobic syringe filter (Advantec, average pore size: 0.1 μm). The filtered solution was analyzed with a ^1H NMR. The concentration of adsorbate is measured by the ratio of the integral of adsorbate and solution.

Overall scheme is subscribed in **Figure 7 and Table 2**. The adsorption kinetics were evaluated by using the pseudo-first-order and pseudo-second-order kinetics models.

(i) Pseudo-first-order kinetics model

The pseudo-first-order adsorption kinetics model is expressed by Eqs. (1).

$$q_t = q_e(1 - e^{-k_1 t}) \quad (1)$$

where q_e (mg g^{-1}) and q_t (mg g^{-1}) are the amounts of adsorbate uptake per mass of adsorbent at equilibrium and at any time t (min). k_1 (min^{-1}) is the rate constant of the pseudo-first-order kinetics model [35].

.(ii) Pseudo-second-order kinetics model

The pseudo-first-order adsorption kinetics model is expressed by Eqs.

(2).

$$q_t = \frac{q_e^2 k_2 t}{1 + k_2 q_e t} \quad (2)$$

where k_2 (min^{-1}) is the rate constant of the pseudo-second-order kinetics model. q_e (mg g^{-1}) and q_t (mg g^{-1}) are the amounts of adsorbate uptake per mass of adsorbent at equilibrium and at any time t (min) which are same meaning in the pseudo-first-order kinetics model [35].

2.5.3. Adsorption isotherms

To determine the maximum adsorption capacities of toxic chemicals, all adsorption isotherm experiments were carried out by a batch method. The adsorption isotherm experiments were divided according to the type of media in which toxic chemicals exist. For adsorption isotherm of quinoline, stock solutions of quinoline with a concentration with 2000 ppm were prepared by dissolving a proper amount of quinoline in n-octane. The solution is diluted to make various concentrations required for the adsorption isotherm experiment (2000, 1000, 500, 250, 125 and 62.5 ppm). The experiments were conducted at room temperature for 12 h in the 50 ml propylene conical tubes by adding 5 mg of synthesized Fe-MIL-88s into the 20 ml of quinoline solution. When the adsorption isotherms experiments were finished, the

particles were filtered with hydrophobic syringe filter (Advantec, average pore size: 0.1 μm). The filtered solution was analyzed with a UV-vis spectroscopy. The UV absorbance at 313 nm was used to calculate the concentrations of quinoline. For adsorption isotherms of 3-MCPD and glycidol, solutions with different concentrations were prepared accordingly. Solutions having various concentrations of adsorbate were used to obtain adsorption isotherms. For adsorption isotherm experiments, 50 mg of Fe-MIL-88s were added into the solution and stirred magnetically at room temperature for 2 h. After adsorption experiments, the solution was separated from the adsorbate with hydrophobic syringe filter (Advantec, average pore size: 0.1 μm). The filtered solution was analyzed with ^1H NMR. The concentration of adsorbate is measured by the ratio of the integral of adsorbate and solution.

Overall scheme is described in **Figure 7 and Table 3**. The adsorption isotherms were explained by using the freundlich and Langmuir isotherms. The freundlich model describes the multilayer adsorption onto heterogeneous surfaces. On the other hand, The Langmuir model describes the monolayer adsorption onto the homogeneous surface and identical affinity for adsorbate on the all the surface. It is also assumed that there is no interaction between adsorbates [36].

(i) Freundlich model

The freundlich model is expressed by Eqs. (3).

$$q_e = K_F C_e^n \quad (3)$$

where q_e (mg g⁻¹) is the amount of adsorbate at equilibrium, C_e (mg L⁻¹) is the adsorbate concentration at equilibrium, K_F is freundlich consatant (mg^{1-(1/n)} L^{1/n} g⁻¹) and n (dimensionless) is freundlich intensity parameter which indicates the magnitude of the surface heterogeneity or the adsorption driving force [37].

(ii) Langmuir model

The pseudo-first-order adsorption kinetics model is expressed by Eqs.

(4).

$$q_t = \frac{Q_{max}^0 K_L C_e}{1 + K_L C_e} \quad (4)$$

where q_e (mg g⁻¹) is the amount of adsorbate at equilibrium, Q_{max}^0 ((mg g⁻¹) is the maximum adsorption capacity of an adsorbent, C_e (mg L⁻¹) is the adsorbate concentration at equilibrium and K_L (L mg⁻¹) is equilibrium constant related to the affinity between an adsorbate and adsorbent [37].

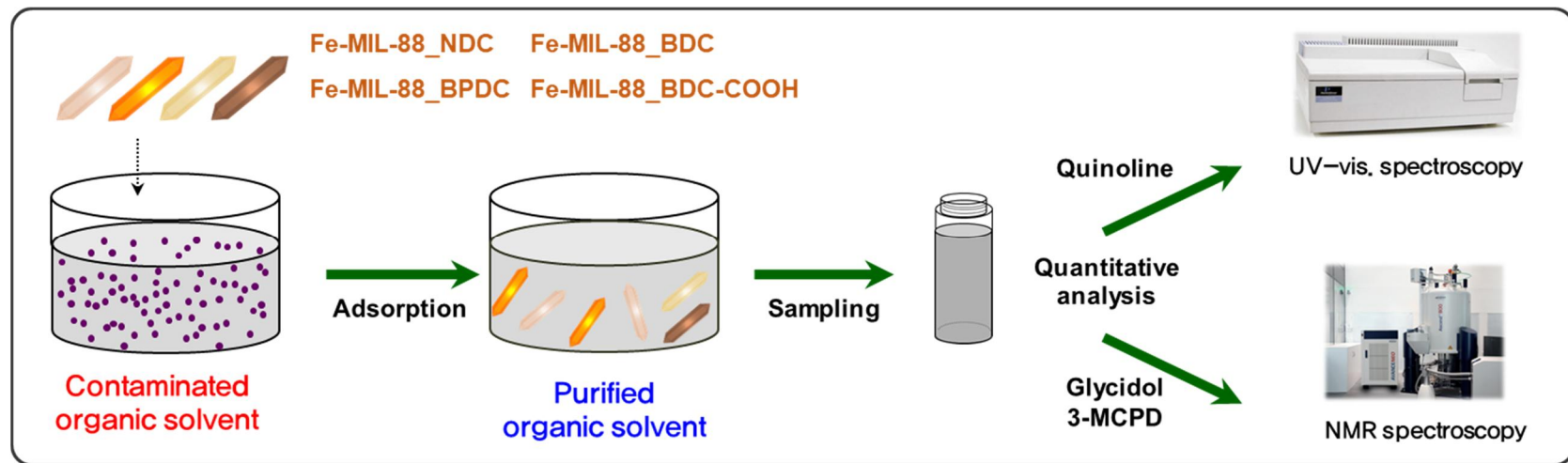


Figure 7. Illustration of adsorption experiments and quantitative analysis of toxic chemicals

Table 2. Adsorption kinetic conditions of toxic chemicals

Adsorbates	Quinoline	Glycidol / 3-MCPD
concentration	50 ppm	10 wt%
Time	5, 15, 30, 60, 120, 720 min	
Temperature	Room temperature	
Rate of stirring	200 rpm	

Table 3. Adsorption isotherm conditions of toxic chemicals

Adsorbates	Quinoline	Glycidol / 3-MCPD
concentration	62.5, 125, 250, 500, 1000, 2000 ppm	2, 4, 6, 8, 10 wt%
Time	720 min	
Temperature	Room temperature	
Rate of stirring	200 rpm	

3. Results and Discussion

3.1. Characteristics of the synthesized Fe-MIL-88s

3.1.1. Structural properties

The positions of the diffraction peaks of the synthesized Fe-MIL-88s were confirmed to be consistent with those reported in the previous studies [30, 31, 38]. It is estimated that d-spacing value of the synthesized Fe-MIL-88s were calculated with the Bragg's law and Scherrer equation (**Table 4**). (001) plane of the crystals indicates the connection of ligands in the Fe-MIL-88 series. The d-spacing value in the (001) plane are arranged according to the length of the ligand (**Figure 8**) [29]. Since the length of the ligand of Fe-MIL-88_BDC was the shortest, the d-spacing value was also the smallest. This means that the distance between lattices is the shortest in the (001) plane [39]. These results indicate that Fe-MIL-88 series was well formed in crystal structure. The order of the d-spacing values of the Fe-MIL-88 series varies depending on the direction of the plane. This affects the tendency of the pore textural properties. **Figure 9 and Figure 10** indicate the nitrogen adsorption-desorption isotherm and BJH desorption cumulative pore volume of various Fe-MIL-88s, respectively. BET surface area, pore volume and average pore

size of various Fe-MIL-88s are displaced in **Table 5**. Although the ligand of Fe-MIL-88_BDC has the shortest length, Fe-MIL-88_NDC had the smallest value in surface area, pore volume and pore size. This is because that organic ligands of Fe-MIL-88_NDC occupy a large area, limiting the surface area and narrowing the pore size. This has been proven by images through computing simulation [27]. Pore textural properties of Fe-MIL-88_BPDC are smaller than that of Fe-MIL-88_BDC due to the smaller geometric surface per volume. As a result, the order of surface area is small in order of Fe-MIL-88_NDC, BPC and BDC [40]. It was confirmed that the surface areas of all Fe-MIL-88 series were less than $10\text{m}^2 \text{ g}^{-1}$. This results can be explained because previous studies have reported that specific surface area of the MIL-88 series is low due to the pore contraction in the dried state [41, 42].

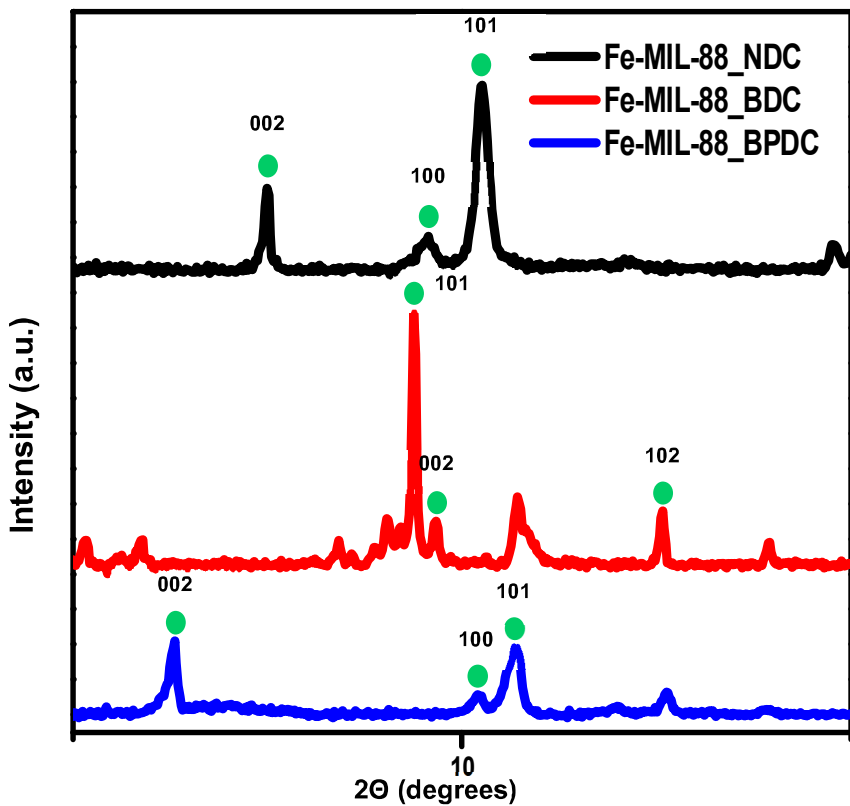


Figure 8. XRD patterns of synthesized Fe-MIL88 series

MOFs	h k l	2Θ (deg.)	d-spacing (nm)	FWHM (2Θ)	Crystallite size (nm)
88_NDC	0 0 2	7.495	1.18	0.107	73.63
88_BDC	0 0 2	9.669	0.91	0.099	79.70
88_BPDC	0 0 2	6.292	1.40	0.095	82.88

Table 4. d-spacing and crystallite size values of the Fe-MIL-88s

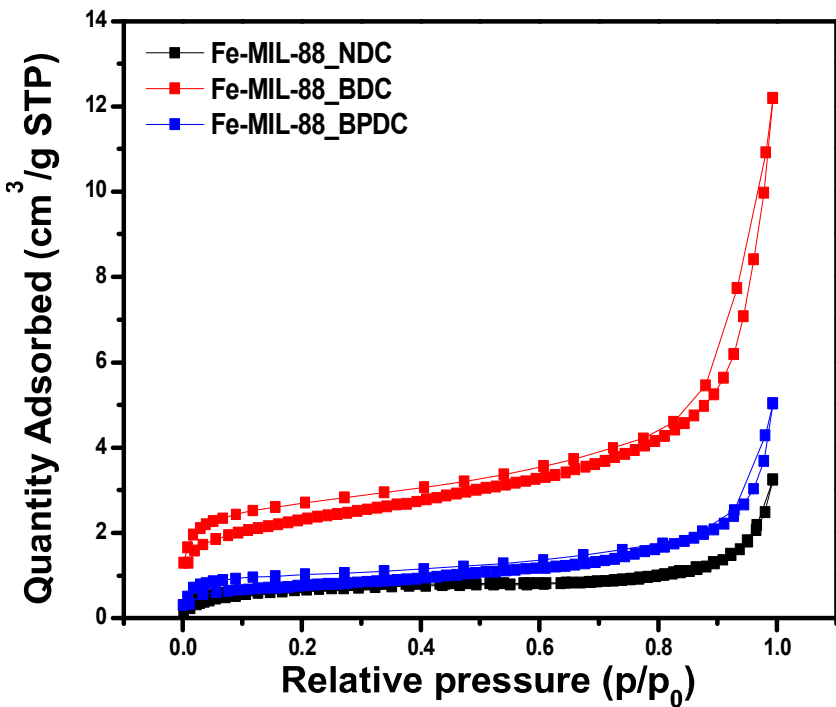


Figure 9. N₂ adsorption-desorption isotherm of various Fe-MIL-88s

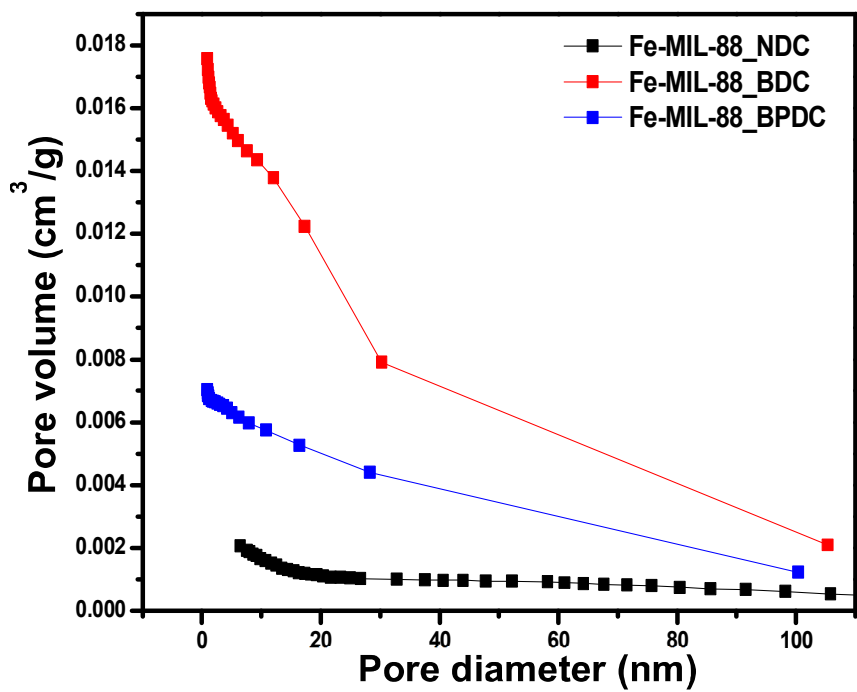


Figure 10. BJH desorption cumulative pore volume of various Fe-MIL-88s

Sample	BET surface area	Pore volume	Average pore size
Fe-MIL-88_NDC	2.576 m ² /g	0.0021 cm ³ /g	1.91 nm
Fe-MIL-88_BDC	8.223 m ² /g	0.0176 cm ³ /g	7.96 nm
Fe-MIL-88_BPDC	2.876 m ² /g	0.0070 cm ³ /g	9.79 nm

Table 5. Surface area and pore size of various Fe-MIL-88s

3.1.2 Morphology

FE-SEM images of the synthesized Fe-ML-88s are shown in **Figure 11**. The morphology of the bipyramidal hexagonal prism were similar to that reported previously [32, 43]. It was found that the shape of bipyramidal hexagonal prism did not change when the ligand type was changed. On the other hand, it was confirmed that the length and thickness of the shape were slightly different. This is probably due to the change of crystal lattice structure by different ligands. Similar to FE-SEM images, bipyramidal hexagonal prism shape was observed through HR-TEM images (**Figure 12**).

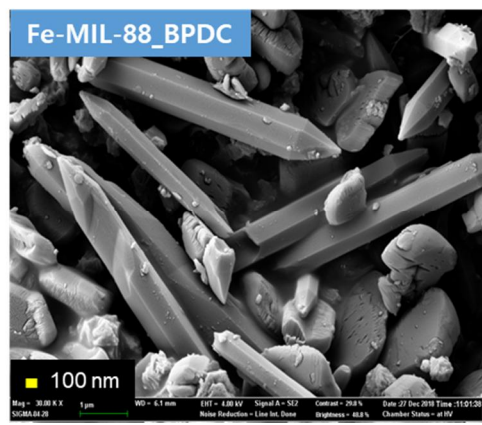
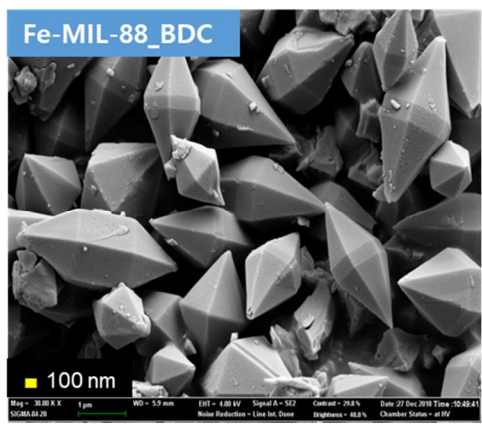
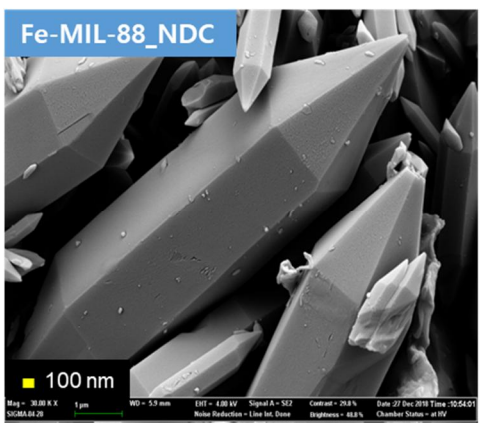
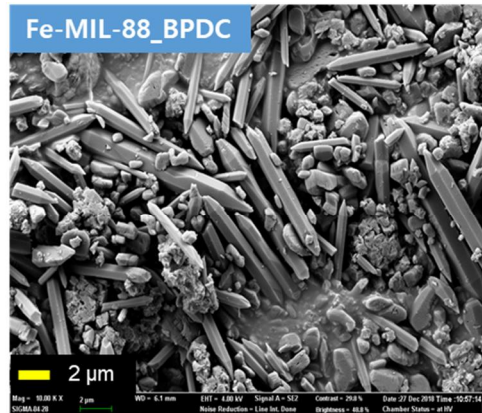
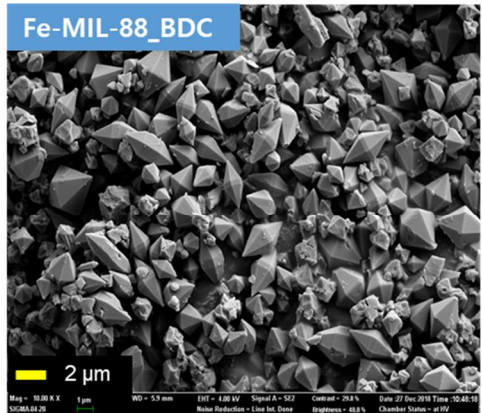
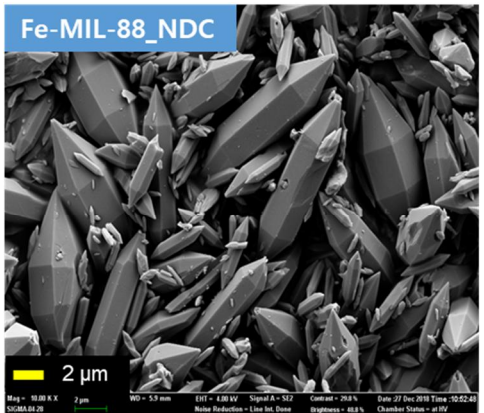


Figure 11. FE-SEM images of the synthesized Fe-MIL-88s

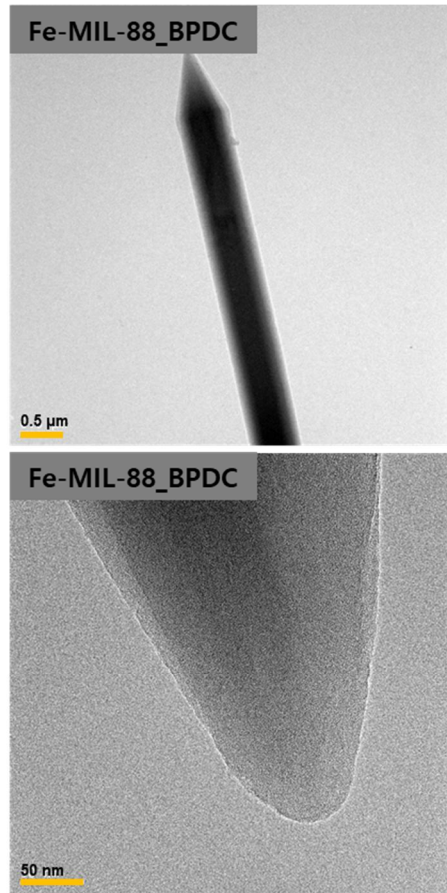
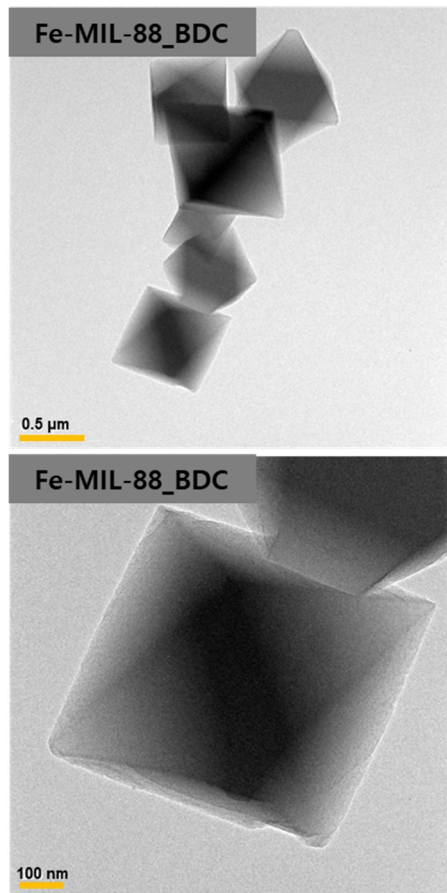
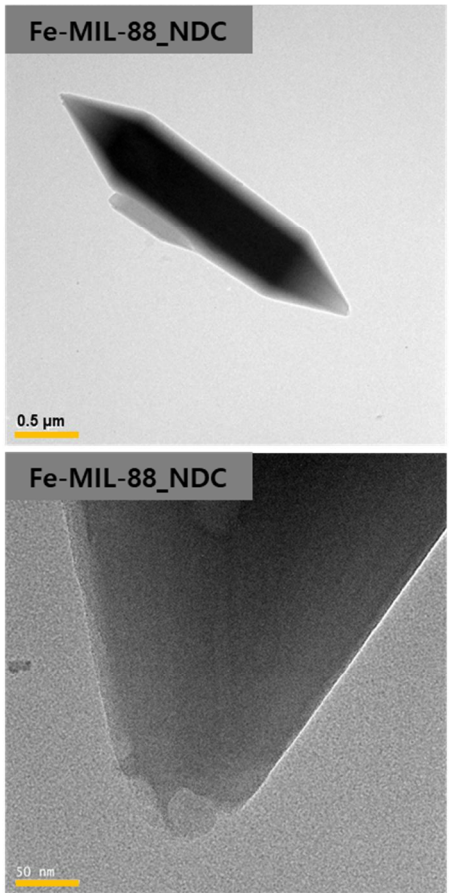


Figure 12. HR-TEM images of the synthesized Fe-MIL-88s

3.1.3 Chemical structure

Figure 13 shows the FT-IR spectra of various Fe-MIL-88s. In case of Fe-MIL-88_NDC, the peaks of 1605 cm^{-1} are assigned to the C=C stretching vibration. In addition, the peaks of 1200 cm^{-1} and 768 cm^{-1} are ascribed to the C-O stretching vibrations and C-H bending, respectively. Also, the peaks of 500 cm^{-1} are related to the Fe-O vibration [44]. In case of Fe-MIL-88_BDC, the characteristics bands at 1599 cm^{-1} and 1390 cm^{-1} are ascribed to the asymmetric and symmetric stretching vibration modes of the coordinating carboxyl groups. Meanwhile, the peaks at 750 cm^{-1} are C-H bending vibration of the aromatic ring. In addition, the peaks of 550 cm^{-1} are ascribed to the Fe-O vibration [45]. Bn The peaks of Fe-MIL-88_BPDC are relatively more varied and complex than that of Fe-MIL-88_N DC and Fe-MIL-88_BDC. The characteristics bands at 1683 cm^{-1} and 1295 cm^{-1} are ascribed to the C=O stretching vibration and C-O stretching vibration. In addition, the peaks of 758 cm^{-1} are ascribed to the C-H bending and the peaks of 550 cm^{-1} are related to the Fe-O stretching [46]. The FT-IR peaks of all synthesized Fe-MIL-88s were consistent with those reported in the literature, confirming that the synthesized samples were chemically coupled well.

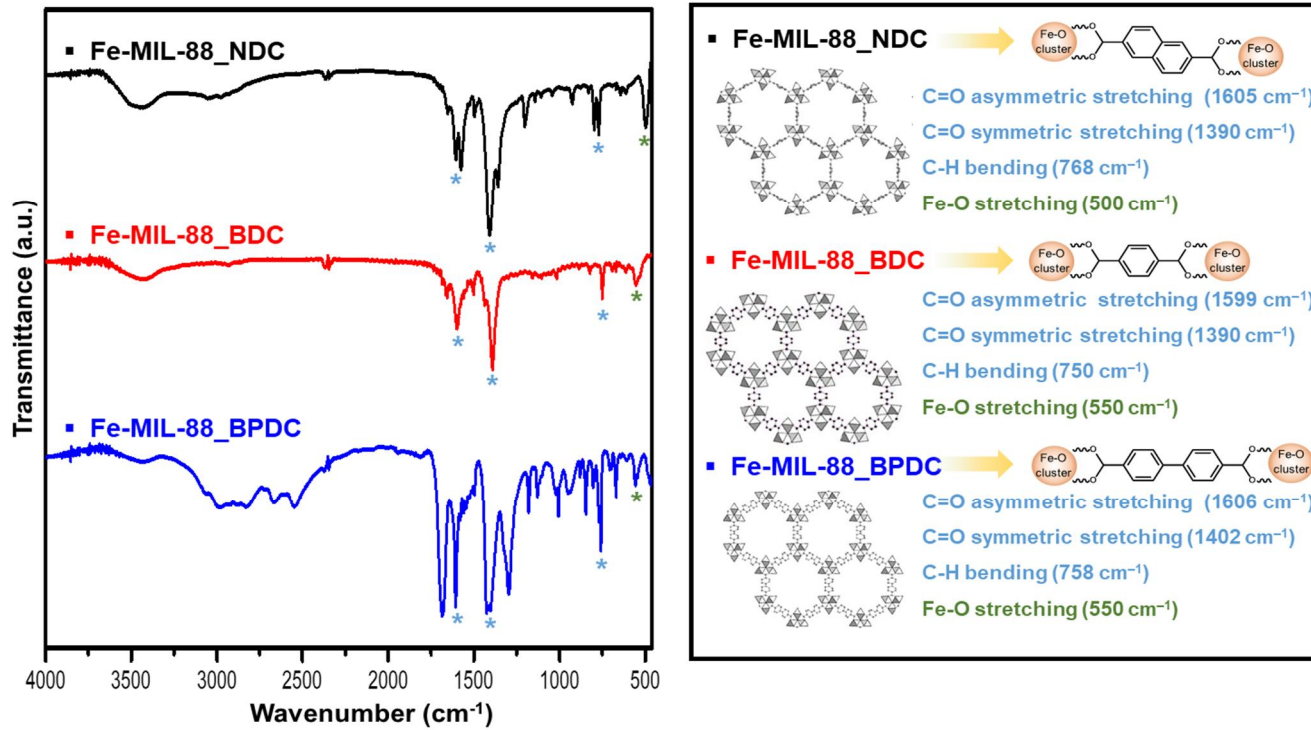


Figure 13. FT-IR spectra of the synthesized Fe-MIL-88s

3.1.4 Thermal behavior

Thermal behaviors of various Fe-MIL-88s are shown in **Figure 14**.

Around 300 °C, weight of the Fe-MIL-88s is decreased rapidly because organic ligands which are forming the structure of the metal organic framework are degraded [42]. In addition, the temperature of 10 % weight loss, T_{d10} , of various Fe-MIL-88s are listed in **Table 6**. The T_{d10} temperatures of Fe-MIL-88_NDC, BDC and BPDC are 310.9 °C, 268.2 °C and 294.9 °C, respectively. From the thermograms and table, It was confirmed that the synthesized Fe-MIL-88s were thermally stable up to about 300 °C. Among them, Fe-MIL-88_BDC was the most thermally stable. Through the thermal analysis of the synthesized Fe-MIL-88s, it was confirmed that these materials have suitable thermal stability to be utilized in the industry.

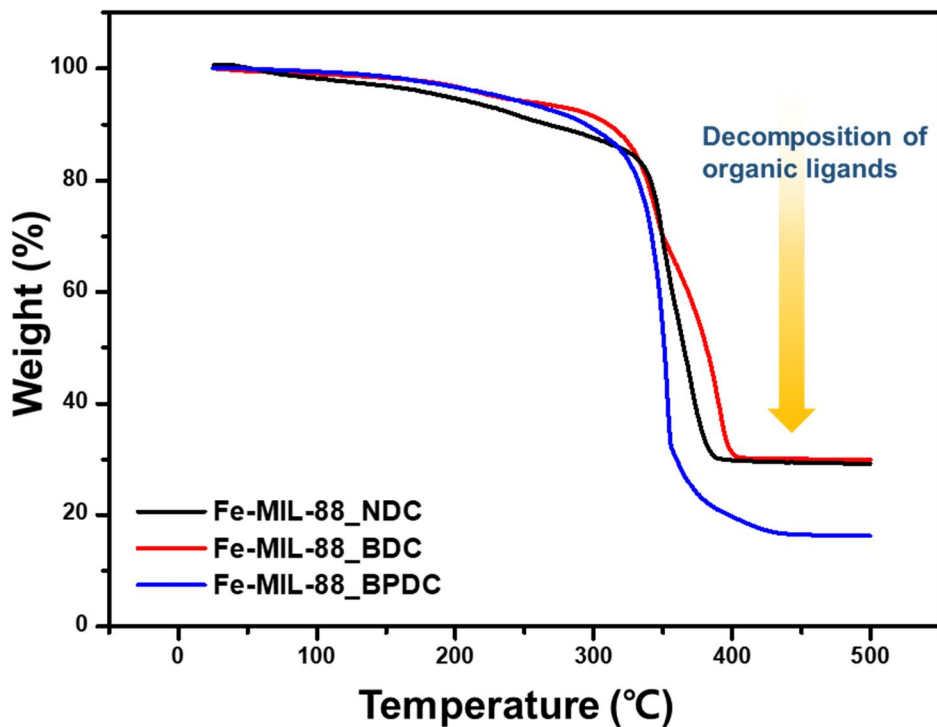


Figure 14. TGA curves of various Fe-MIL-88s

Sample	T _{d10} (°C)
Fe-MIL-88_NDC	268.2
Fe-MIL-88_BDC	310.9
Fe-MIL-88_BPDC	294.9

Table 6. Td10 (10 % weight loss temperature) of various Fe-MIL-88s

3.2. Evaluation of adsorption performance of various Fe-MIL-88s toward toxic chemicals

3.2.1. Adsorption kinetics

The effect of contact time between quinoline and Fe-MIL-88 series was examined for investigating adsorption rate of Fe-MIL-88 series for quinoline. As shown in **Figure 15**, the adsorption capacity reaches equilibrium within 120 minutes. To further analyze the adsorption kinetics of quinoline adsorption onto Fe-MIL-88s, the data was fitted to two kinetic models; pseudo-first order model and pseudo-second order model. As listed in **Table 7**, the results indicate that adsorption of quinoline on Fe-MIL-88s is fitted to the pseudo-second order kinetic model by comparing the values of correlation coefficient (R^2). By the comparison of k_2 values of pseudo-second order equation, the q_e values of Fe-MIL-88_BDC indicated that the adsorption for quinoline onto the Fe-MIL-88_BDC is the fastest. Adsorption capacity was also highest in Fe-MIL-88_BDC. This result shows that Fe-MIL-88_BDC has the highest surface area and pore volume, which means that the largest number of open metal sites can have an acid-base interaction with quinoline.

To identify the rate of adsorption for 3-MCPD and glycidol, the effect of

contact time on 3-MCPD and glycidol removal by the synthesized Fe-MIL-88s were shown in **Figure 16 and 17**. In the case of both adsorbates, the adsorption equilibrium onto the synthesized Fe-MIL-88s was achieved within 2 hours. In addition, the order of adsorption amount was in the order of Fe-MIL-88_BDC, BPDC and NDC for both adsorbents. To further analyze the adsorption kinetics of 3-MCPD and glycidol adsorption onto Fe-MIL-88s, the data was fitted to two kinetic models; pseudo-first order model and pseudo-second order model. The parameters of pseudo-first order kinetic and pseudo-second order kinetic model were listed in **Table 8**. Both adsorption kinetics of 3-MCPD and glycidol onto Fe-MIL-88s were fitted in pseudo-second order kinetic model with a correlation coefficient. Comparing the k_2 value from pseudo-second order equation of three Fe-MIL-88s, it was confirmed that Fe-MIL-88_BDC has a high adsorption rate for both adsorbates. In addition, similar to adsorption of quinoline, Fe-MIL-88_BDC had the highest adsorption performance. This is because the surface area and pore volume of Fe-MIL-88_BDC are the highest, there are a lot of sites for van der waals interaction with 3-MCPD and glycidol. From these results, it can be seen that the adsorption rate and capacity appear in order to the tendency of the surface area and pore volume.

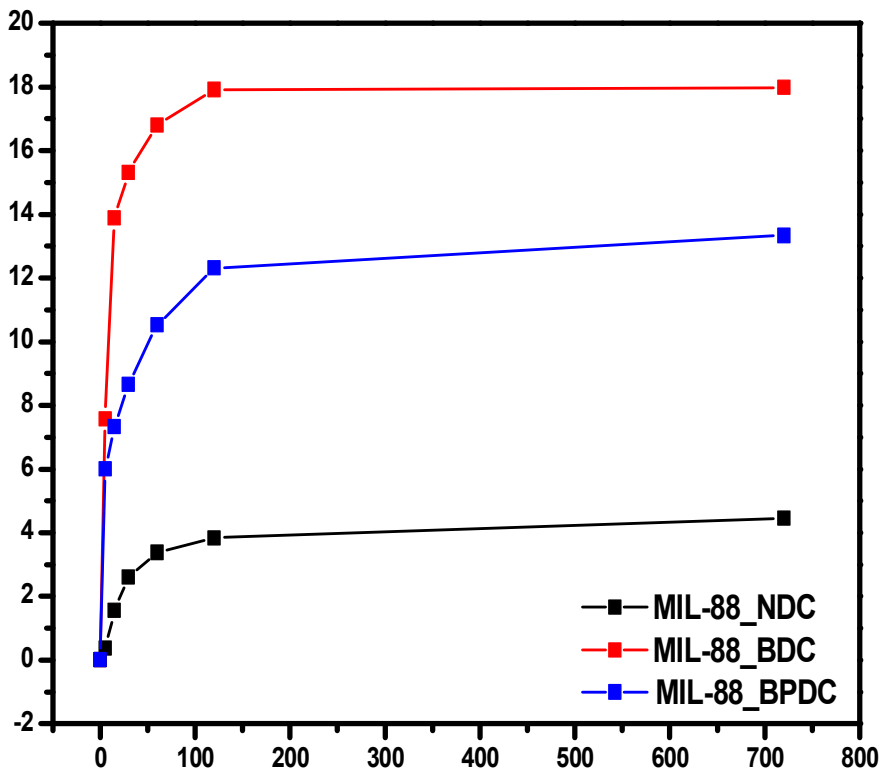


Figure 15. Adsorption kinetics of quinoline uptakes in various Fe-MIL-88s

Table 7. Kinetic parameters of the pseudo-first order model; (a) and the pseudo-second order model; (b) for quinoline adsorption

PFO equation	q_e	k_I	R^2
Fe-MIL-88_NDC	4.2239	0.0289	0.9867
Fe-MIL-88_BDC	17.262	0.1067	0.9872
Fe-MIL-88_BPDC	11.809	0.0695	0.8697

(a)

PFO equation	q_e	k_I	R^2
Fe-MIL-88_NDC	4.7259	0.0077	0.9875
Fe-MIL-88_BDC	18.587	0.0086	0.9941
Fe-MIL-88_BPDC	12.793	0.0084	0.9516

(b)

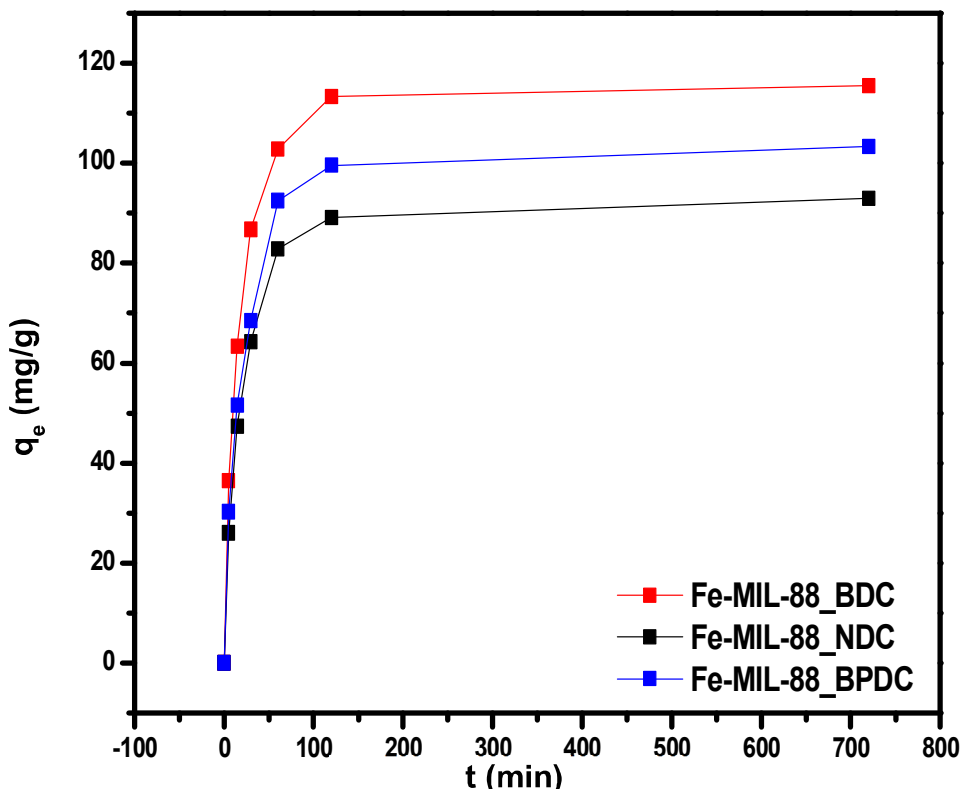


Figure 16. Adsorption kinetics of 3-MCPD uptakes in various Fe-MIL-88s

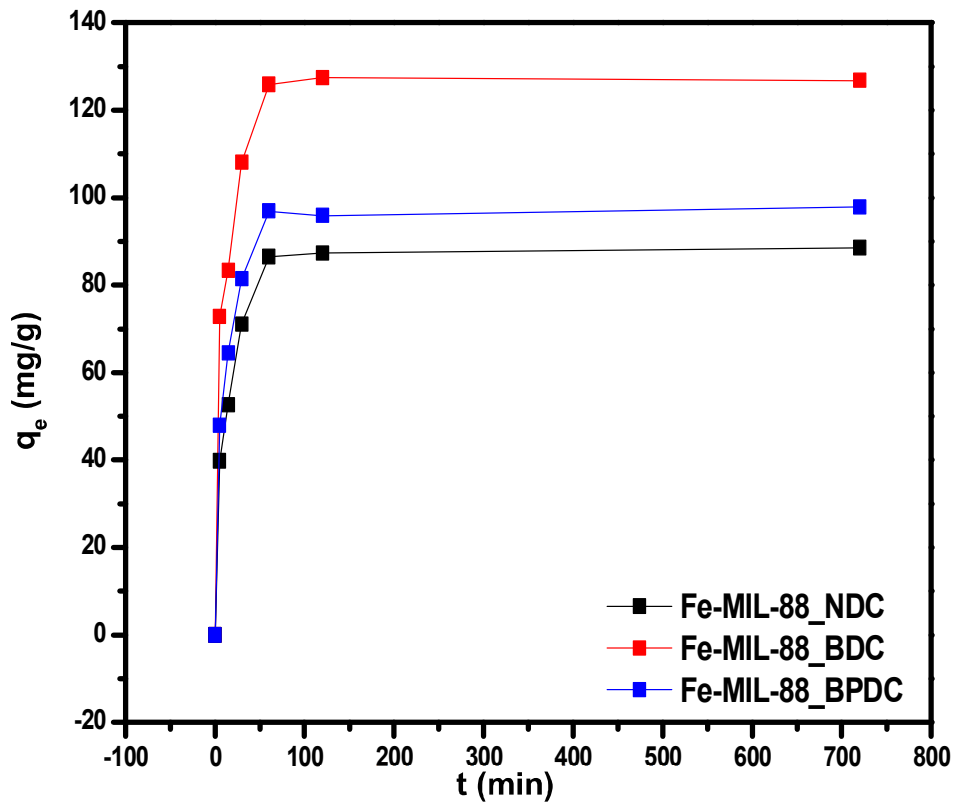


Figure 17. Adsorption kinetics of glycidol uptakes in various Fe-MIL-88s

Table 8. Kinetic parameters of the pseudo-first order model and the pseudo-second order model for 3-MCPD and glycidol adsorption

3-MCPD	Pseudo-first order kinetic model			Pseudo-second order kinetic model		
	q _e	k ₁	R ²	q _e	k ₂	R ²
Fe-MIL-88_NDC	89.714	0.0480	0.9867	97.791	0.0007	0.9938
Fe-MIL-88_BDC	111.406	0.0564	0.9846	121.060	0.0007	0.9954
Fe-MIL-88_BPDC	100.148	0.0457	0.9800	108.899	0.0006	0.9890
Glycidol	q _e	k ₁	R ²	q _e	k ₂	R ²
Fe-MIL-88_NDC	86.167	0.0748	0.9547	92.038	0.0013	0.9791
Fe-MIL-88_BDC	121.643	0.1165	0.9214	129.398	0.0016	0.9703
Fe-MIL-88_BPDC	94.382	0.0951	0.9561	100.702	0.0016	0.9856

3.2.2. Adsorption isotherms

As shown in **Figure 18**, All Fe-MIL-88 series showed that the adsorption capacity of quinoline increases as the initial concentration of quinoline increases. To further analyze the adsorption isotherms of quinoline adsorption onto Fe-MIL-88s, the data from adsorption isotherm experiments were fitted to the two isotherm models: Freundlich model and Langmuir model. The fitting parameters were listed in **Table 8**. From the value of correlation coefficient (R^2), adsorption isotherms of quinoline onto the synthesized Fe-MIL-88s were better fitted to the langmuir model than freundlich model. Therefore, adsorption for quinoline onto the various Fe-MIL-88s is a monolayer adsorption on homogenous surfaces. Comparing the value of Q_{max}^0 from langmuir model, Fe-MIL-88_BDC exhibits the highest quinoline uptakes. This is because the higher surface area and pore volume, the more open metal sites can interact with quinoline. This can lead to more acid-base interactions.

To evaluate the adsorption isotherms of 3-MCPD and glycidol, batch adsorption experiments were conducted at room temperature with initial concentration from 2 to 10 wt %. The adsorption isotherms of 3-MCPD and glycidol onto various Fe-MIL-88s were shown in **Figure 19 and 20**. In the cases of both 3-MCPD and glycidol adsorption, adsorption amounts at Fe-MIL-88_BDC were the highest among the three synthesized Fe-MIL-88s.

The parameters of the Freundlich and Langmuir model were listed in **Table 9**. In the case of both 3-MCPD and glycidol adsorption, the value of correlation coefficient of Langmuir model was higher than the value of Freundlich model. Therefore, 3-MCPD and glycidol adsorption onto various Fe-MIL-88s were fitted with the Langmuir model. From this result, 3-MCPD and glycidol adsorption onto Fe-MIL-88s is a monolayer adsorption on a homogeneous surfaces and Fe-MIL-88_BDC exhibits the highest 3-MCPD and glycidol uptakes as in the quinoline adsorption. The higher the surface area, the more van der waals interactions can be induced. These results confirmed that Fe-MIL-88_BDC had the best adsorption capacity for toxic chemicals in oily phase.

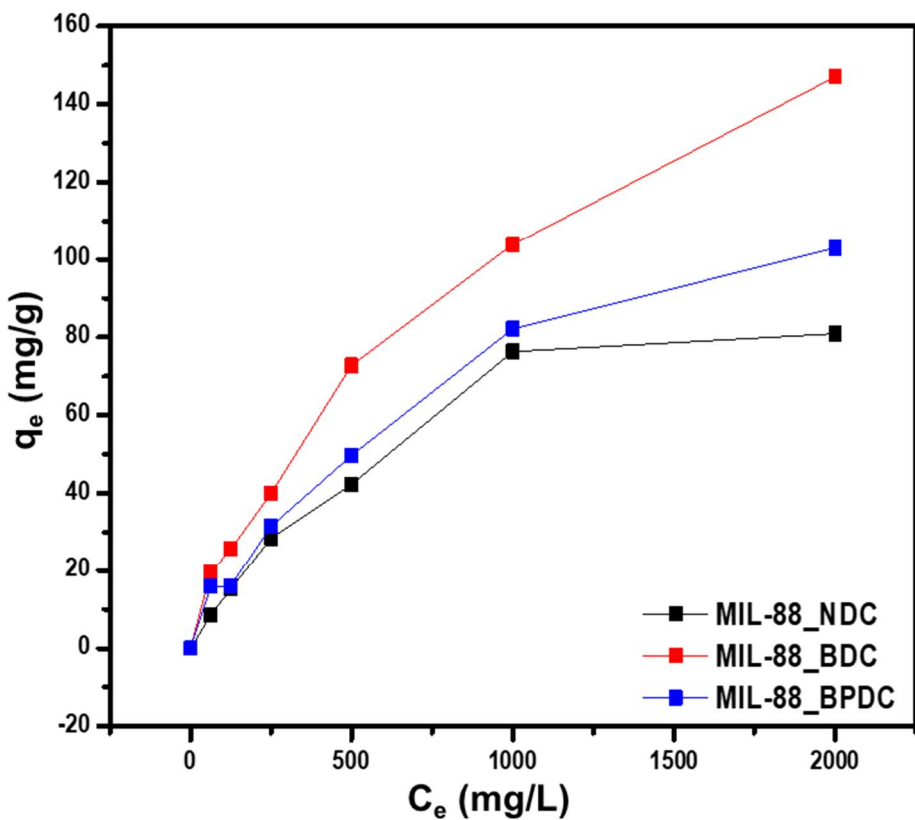


Figure 18. Adsorption isotherms of quinoline uptakes in various Fe-MIL-88s

Table 8. Isotherm parameters of the Freundlich model; (a) and Langmuir model; (b) for quinoline adsorption

Freundlich	K_f	n	R^2
Fe-MIL-88_NDC	1.5586	0.5318	0.9090
Fe-MIL-88_BDC	1.7846	0.5830	0.9902
Fe-MIL-88_BPDC	1.4820	0.5638	0.9703

(a)

Langmuir	Q_{max}^0	K_L	R^2
Fe-MIL-88_NDC	117.4	0.0013	0.9747
Fe-MIL-88_BDC	222.3	0.0009	0.9941
Fe-MIL-88_BPDC	153.5	0.0011	0.9906

(b)

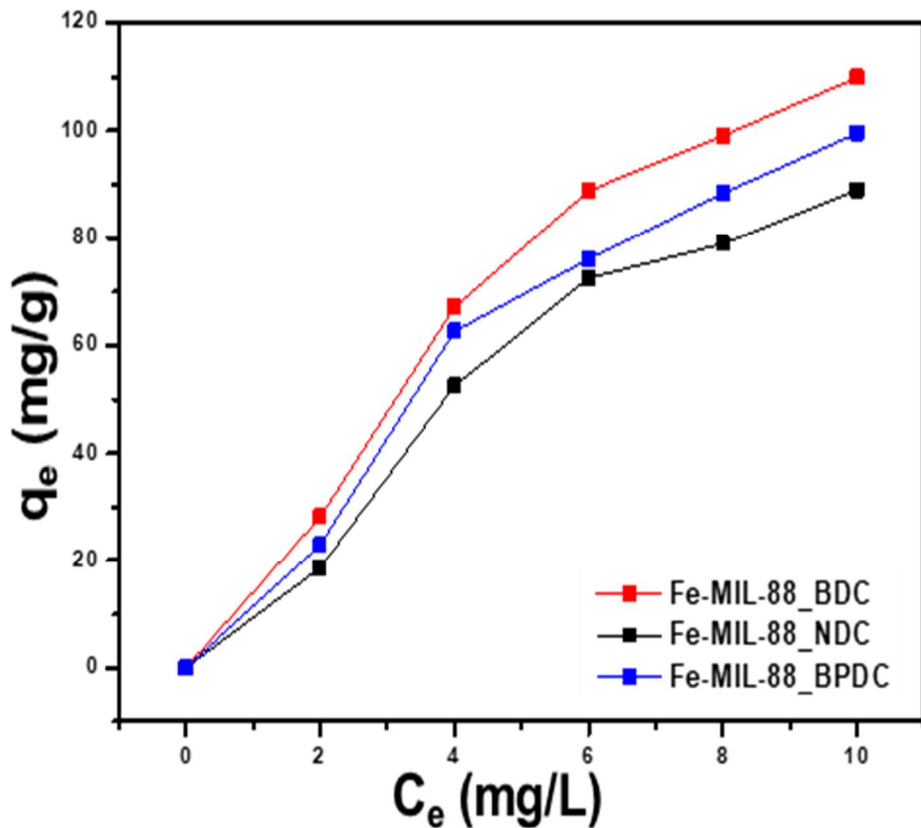


Figure 19. Adsorption isotherms of 3-MCPD uptakes in various Fe-MIL-88s

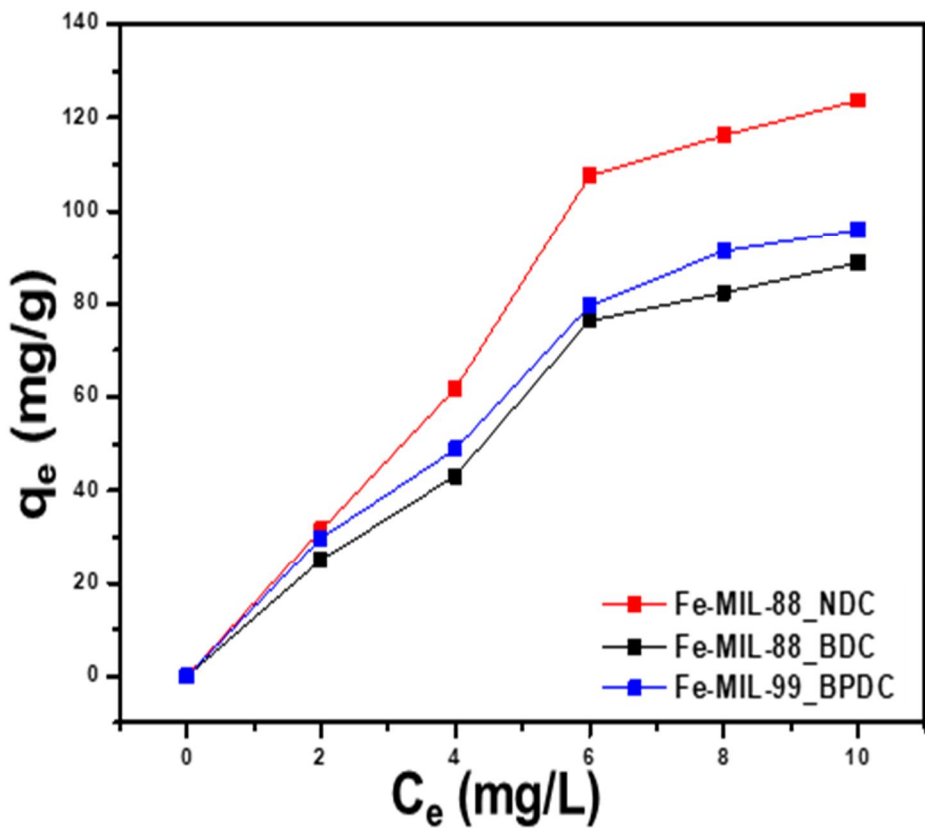


Figure 20. Adsorption isotherms of glycidol uptakes in various Fe-MIL-88s

Table 9. Isotherm parameters of the Freundlich model and Langmuir model for 3-MCPD and glycidol

3-MCPD	Freundlich isotherm model			Langmuir isotherm model		
	K _f	n	R ²	Q _{max} ^o	K _L	R ²
Fe-MIL-88_NDC	17.286	0.734	0.9090	214.551	0.074	0.9721
Fe-MIL-88_BDC	23.952	0.682	0.9302	233.969	0.093	0.9840
Fe-MIL-88_BPDC	20.504	0.702	0.9212	220.412	0.085	0.9780
Glycidol	K _f	n	R ²	Q _{max} ^o	K _L	R ²
Fe-MIL-88_NDC	17.500	0.733	0.9088	224.792	0.070	0.9692
Fe-MIL-88_BDC	22.536	0.690	0.9422	232.791	0.087	0.9872
Fe-MIL-88_BPDC	20.157	0.704	0.9366	226.914	0.079	0.9817

adsorption

3.3. Characteristics of the carboxyl-functionalized Fe-MIL-88_BDC

3.3.1. Structural property

The characteristic peaks of Fe-MIL-88_BDC-NH₂ were clearly observed as shown in **Figure 21** [47]. The pattern sharpness indicates a high degree of crystallinity of the space group and structure without other peaks. This means that pure Fe-MIL-88_BDC-NH₂ were obtained. The XRD pattern of MOFs maintains the same pattern after the post synthetic modification reaction [48]. The patterns are identical after carboxyl-functionalization of Fe-MIL-88_BDC-NH₂ and confirm the successful synthesis of Fe-MIL-88_BDC-COOH. However, the intensity of the XRD peaks is lower than that of Fe-MIL-88_BDC due to the post modification with pore filling. This means that the crystallinity is relatively lower than that of Fe-MIL-88_BDC-NH₂ [48]. This result also supported the data of textural properties. **Figure 22 and Figure 23** indicate the N₂ adsorption-desorption isotherm and BJH desorption cumulative pore volume of various Fe-MIL-88_BDC-NH₂ and BDC-COOH, respectively. BET surface area, pore volume and average pore size of Fe-MIL-88_BDC-NH₂ and COOH are displaced in **Table 10**. Comparing of Fe-MIL-88_BDC-NH₂ and BDC-COOH, it was confirmed that the surface area, pore volume and average pore size of Fe-MIL-

88_BDC-COOH were slightly decreased due to the post modification [49]. Comparing Fe-MIL-88_BDC and functionalized Fe-MIL-88_BDC, the introduction of functional groups reduced the extent of pore contraction, which led to an increase in pore size and surface area [50, 51].

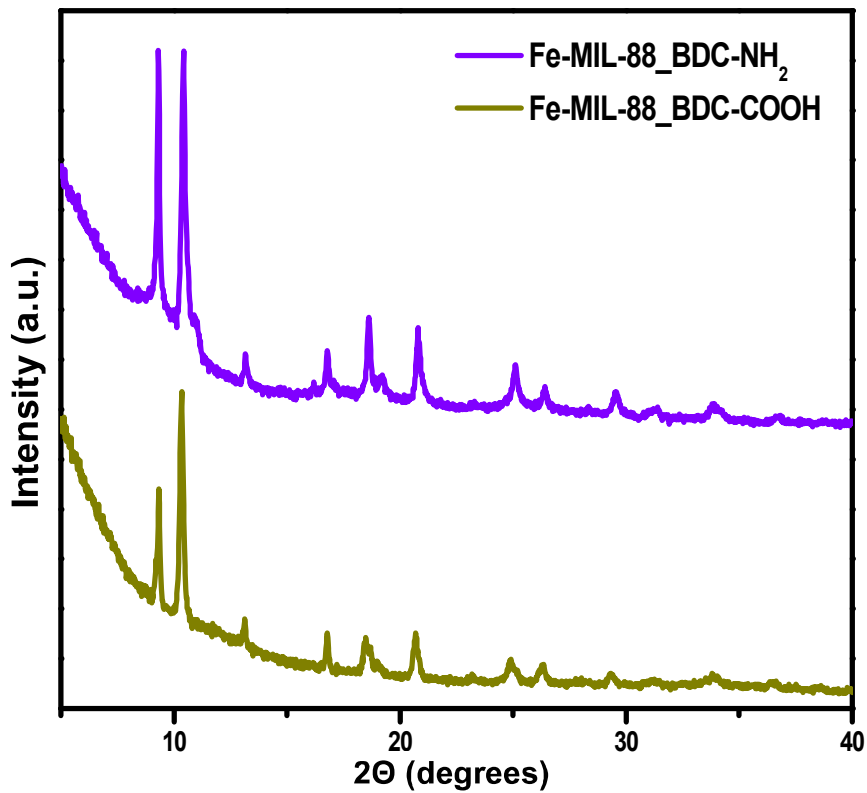


Figure 21. XRD patterns of synthesized Fe-MIL-88_BDC-NH₂

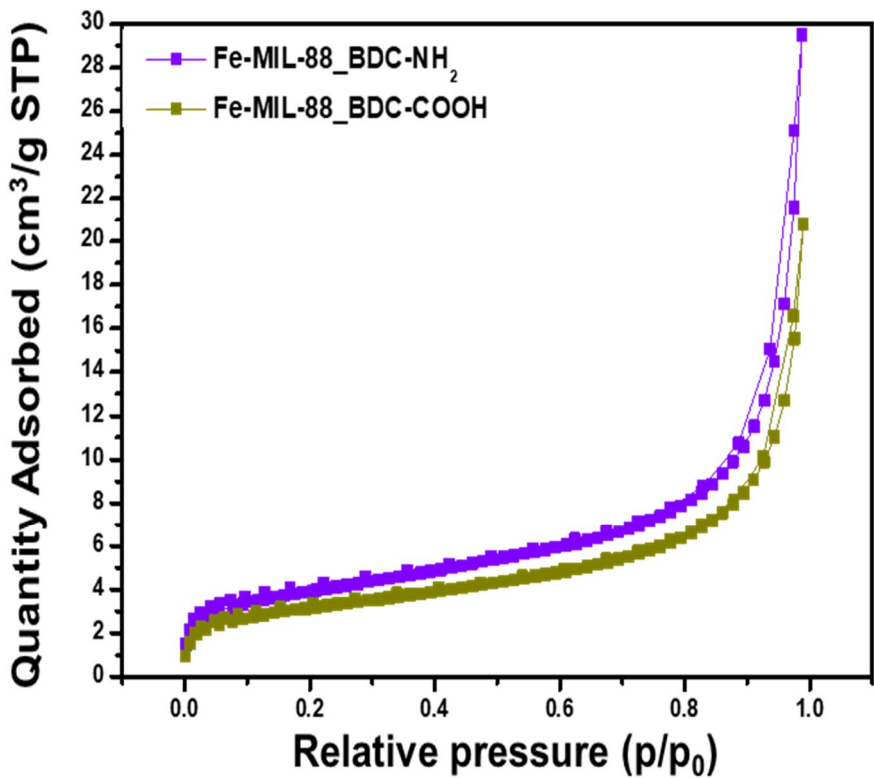


Figure 22. N_2 adsorption-desorption isotherm of Fe-MIL-88_BDC-NH₂ and BDC-COOH

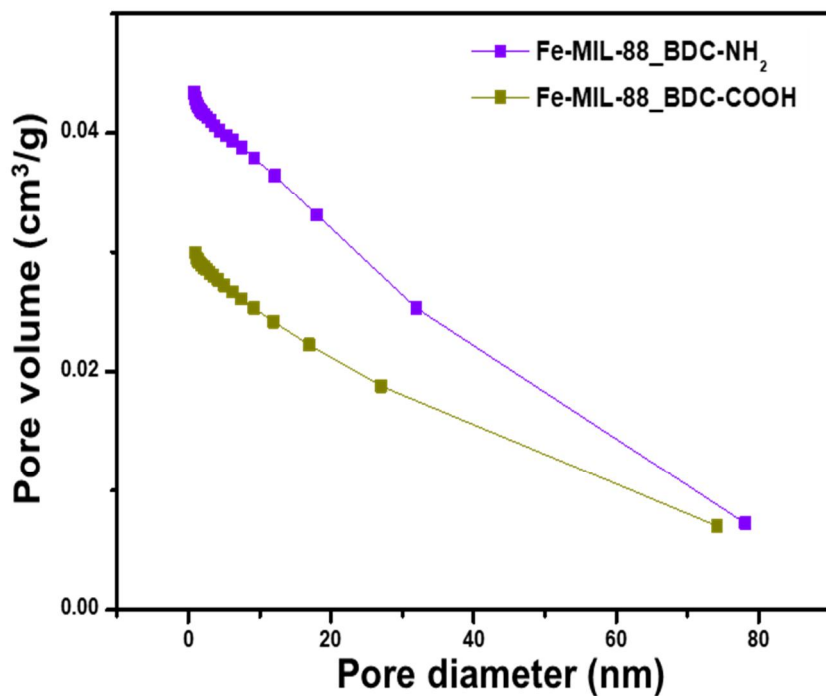


Figure 23. BJH desorption cumulative pore volume of Fe-MIL-88_BDC-NH₂ and BDC-COOH

Sample	BET surface area	Pore volume	Average pore size
Fe-MIL-88_BDC-NH ₂	13.740 m ² /g	0.0434 cm ³ /g	12.14 nm
Fe-MIL-88_BDC-COOH	11.162 m ² /g	0.0299 cm ³ /g	11.83 nm

Table 10. Textural properties of Fe-MIL-88_BDC-NH₂ and BDC-COOH

3.3.2. Morphology

The morphology of the functionalized Fe-MIL-88s were observed by FE-SEM images as shown in **Figure 23**. The shape uniformity of functionalized Fe-MIL-88_BDC was reduced compared to the unmodified Fe-MIL-88_BDC. This is because of the effect of functionalization and bulky synthesis in grams without the use of acids such as hydrofluoric acid [52]. Hydrofluoric acid can act as a modulator for controlling morphology due to the strong electronegativity of fluoride anions. These anions affect the binding of MOFs to regulate crystal nucleation and growth [53]. However, Similar to the unmodified Fe-MIL-88s, The functionalized Fe-MIL-88s are spindle-shaped [54]. The size of functionalized Fe-MIL-88s lie in the range of 2 μm to 5 μm . From these results, the morphology of functionalized Fe-MIL-88s is well indicated as reported in the reported literatures [33].

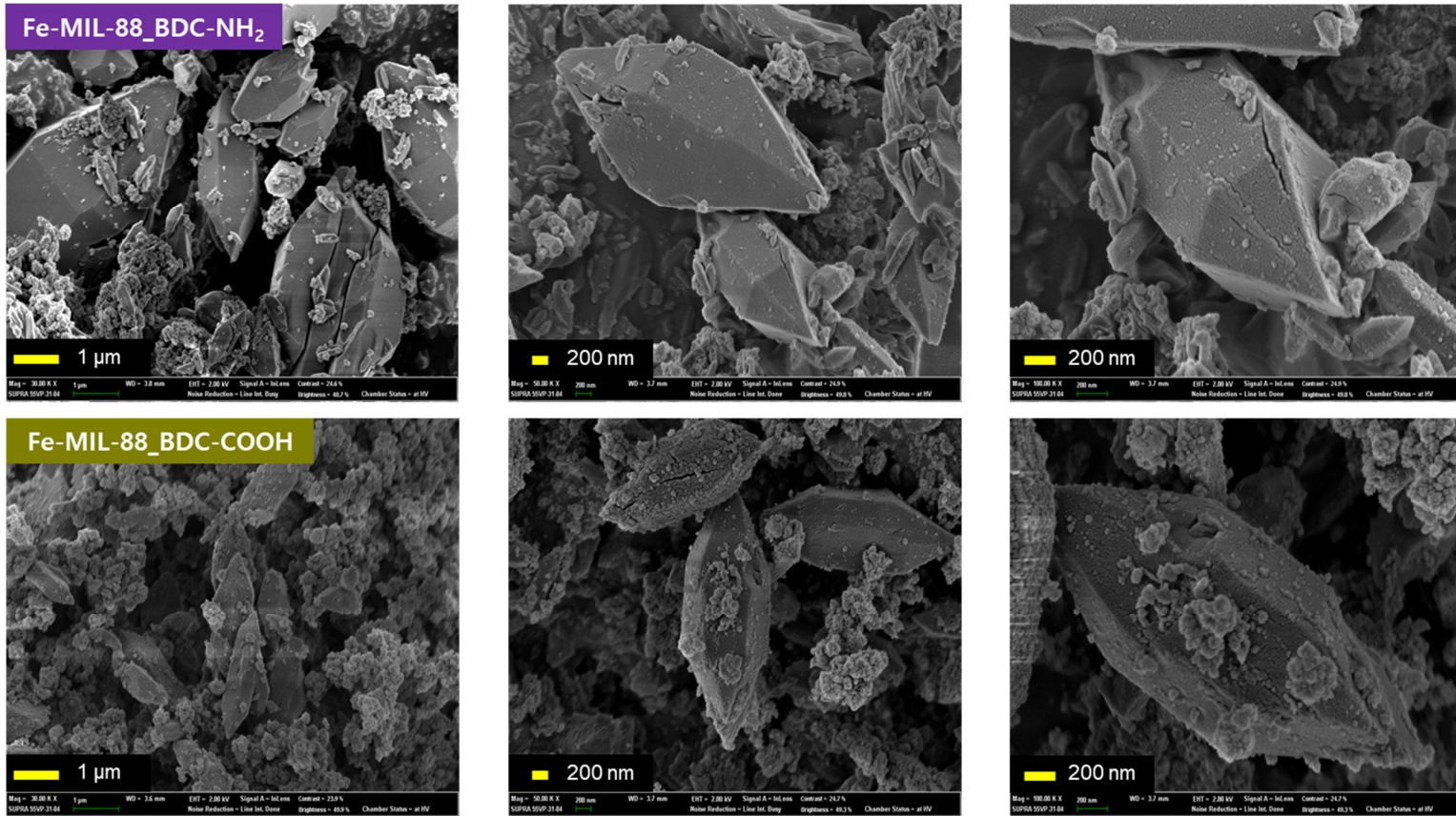


Figure 23. FE-SEM images of the Fe-MIL-88_BDC-NH₂ and Fe-MIL-88_BDC-COOH

3.3.3. Chemical structure

In the case of Fe-MIL-88_BDC-NH₂, as shown in **Figure 26**, the characteristic bands at 3421 cm⁻¹ and 3348 cm⁻¹ are ascribed to the asymmetric and symmetric stretching vibrations of the N-H band. Bending vibration of the N-H band has appeared at 1654 cm⁻¹. The band at 750 cm⁻¹ is attributed to the C-H bending vibration of the aromatic ring. The presence of peaks of 500 cm⁻¹ are related to the Fe-O vibration [45]. The positions of all characteristic peaks indicated that Fe-MIL-88_BDC-NH₂ was successfully synthesized. For Fe-MIL-88_BDC-COOH, some additional peaks are directly observed. The peaks at 3288 cm⁻¹ are associated with the N-H stretching vibrations of secondary amide. The characteristics bands at 1710 cm⁻¹ are ascribed to the C=O stretching band of -COOH group from carboxylic acid. C=O stretching of secondary amide exhibited characteristic peaks at 1680 cm⁻¹. Similar to Fe-MIL-88_BDC-NH₂, the characteristic peaks of Fe-O vibrations were located at 500 cm⁻¹. Moreover, decreasing intensity of asymmetric and symmetric N-H band means that amide bonds were well formed. From these results, carboxyl functional groups were successfully introduced into the organic ligands.

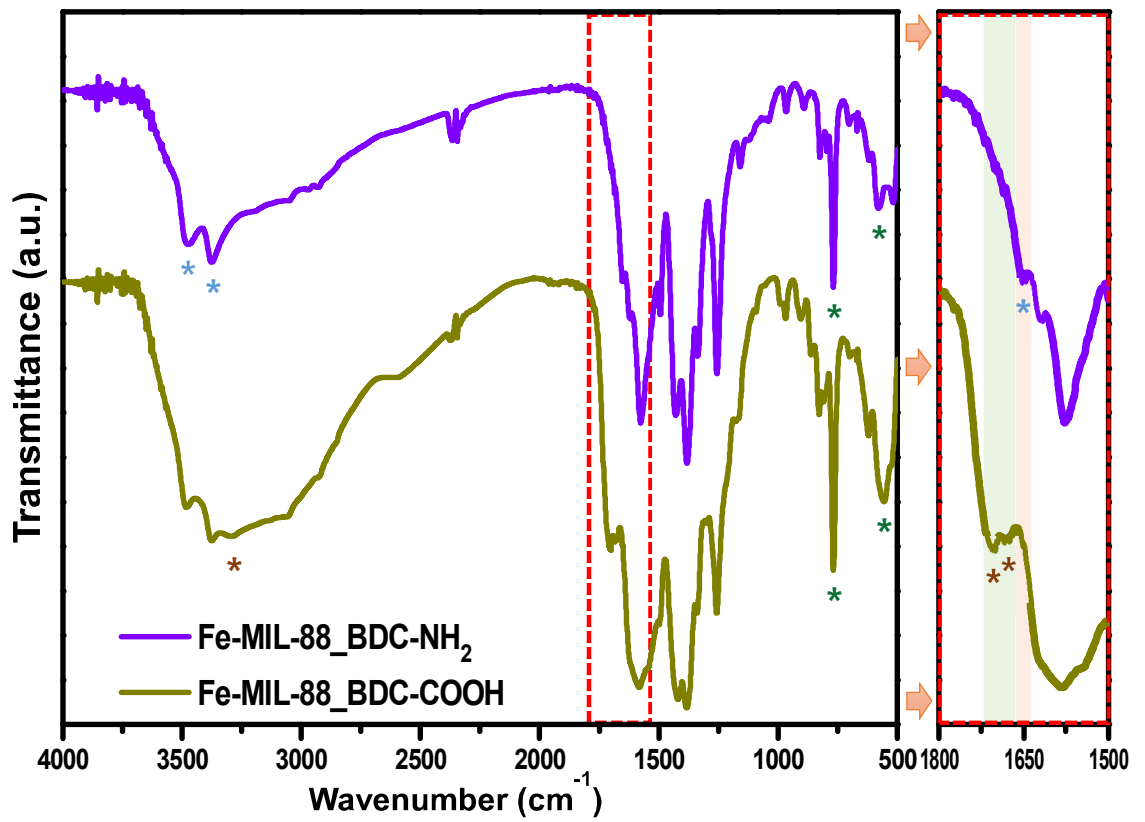


Figure 26. FT-IR spectra of the Fe-MIL-88_BDC-NH₂ and Fe-MIL-88_BDC-COOH

3.3.4. Thermal behavior

Thermal behaviors of Fe-MIL-88_BDC-NH₂ and Fe-MIL-88_BDC-COOH are shown in **Figure 27**. Initial weight loss occurred up to 250 °C, indicating the evaporation of the residual solvents and organic functional group. The TGA curve shows second weight loss in the range of 250 – 400 °C, derived from the partial cracking of the organic ligand of the Fe-MIL-88_BDC-NH₂ and Fe-MIL-88_BDC-COOH. T_{d10} of various Fe-MIL-88_BDC-NH₂ and Fe-MIL-88_BDC-COOH are listed in **Table 11**. There is little difference between the value of T_{d10} of two samples. Thermal stability is relatively reduced compared to T_{d10} of unmodified Fe-MIL-88_BDC. This results are due to the increased number of defects by functionalization. Although the thermal stability is reduced, the functionalized Fe-MIL-88_BDC also has a suitable thermal stability for industrial use.

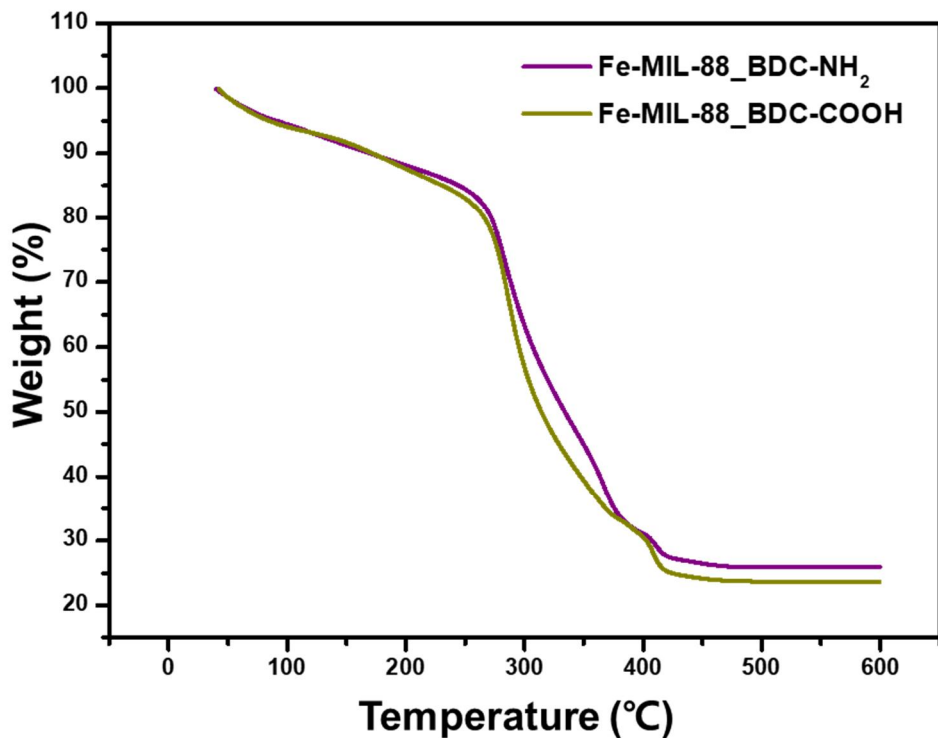


Figure 27. TGA curves of Fe-MIL-88_BDC-NH₂ and Fe-MIL-88_BDC-COOH

Sample	T _{d10} (°C)
Fe-MIL-88_BDC-NH ₂	170.0
Fe-MIL-88_BDC-COOH	172.1

Table 11. of Fe-MIL-88_BDC-NH₂ and Fe-MIL-88_BDC-COOH

3.4. Evaluation of adsorption performance of carboxyl-functionalized Fe-MIL-88_BDC

3.4.1. Adsorption kinetics

To confirm the effect of time on the adsorption of toxic chemicals onto Fe-MIL-88_BDC-COOH, batch experiments were conducted. As shown in **Figure 28, 29 and 30**, the adsorption capacity rapidly increases since the equilibrium is almost reached after 120 min. In order to further analyze adsorption kinetics of toxic chemicals, pseudo-first-order kinetic model and pseudo-second-order kinetic model were used to fit the experimental data. It is clear that the pseudo-second-order kinetic model is suitable to describe the experimental data by comparing correlation coefficient (R^2). **Table 12 and 13** indicates the fitting parameters of kinetic models for adsorption of toxic chemicals. Comparing of k_2 , which is defined as the pseudo-second-order rate constants, of two adsorbents, the adsorption rate of Fe-MIL-88_BDC-COOH is faster than that of Fe-MIL-88_BDC. In addition, the adsorption capacity of carboxyl-functionalized Fe-MIL-88_BDC are higher than that of the conventional Fe-MIL-88_BDC. These results are due to the additional interaction between carboxyl-functionalized ligands and toxic and high

surface area.

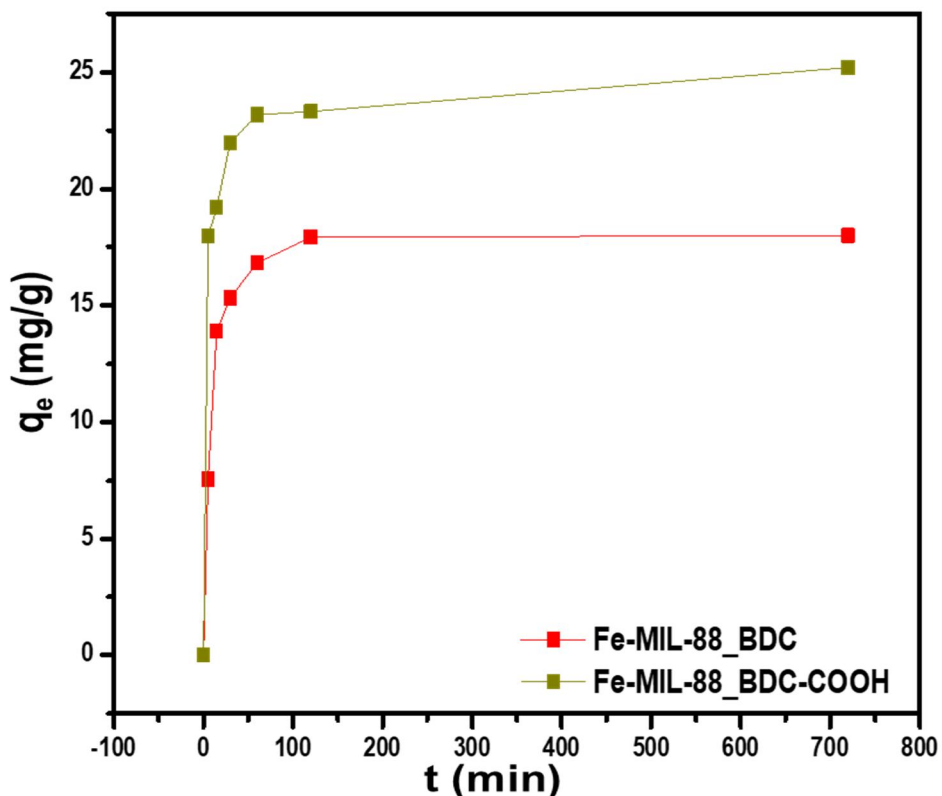


Figure 28. Adsorption kinetics of quinoline uptakes in Fe-MIL-88_BDC and Fe-MIL-88_BDC-COOH

Table 12. Kinetic parameters of the pseudo-first order model; (a) and the pseudo-second order model; (b) for quinoline adsorption

PFO equation	q_e	k_I	R^2
Fe-MIL-88_BDC	17.262	0.1067	0.9872
Fe-MIL-88_BDC-COOH	22.731	0.2905	0.9518

(a)

PFO equation	q_e	k_I	R^2
Fe-MIL-88_BDC	18.587	0.0086	0.9941
Fe-MIL-88_BDC-COOH	23.918	0.0202	0.9829

(b)

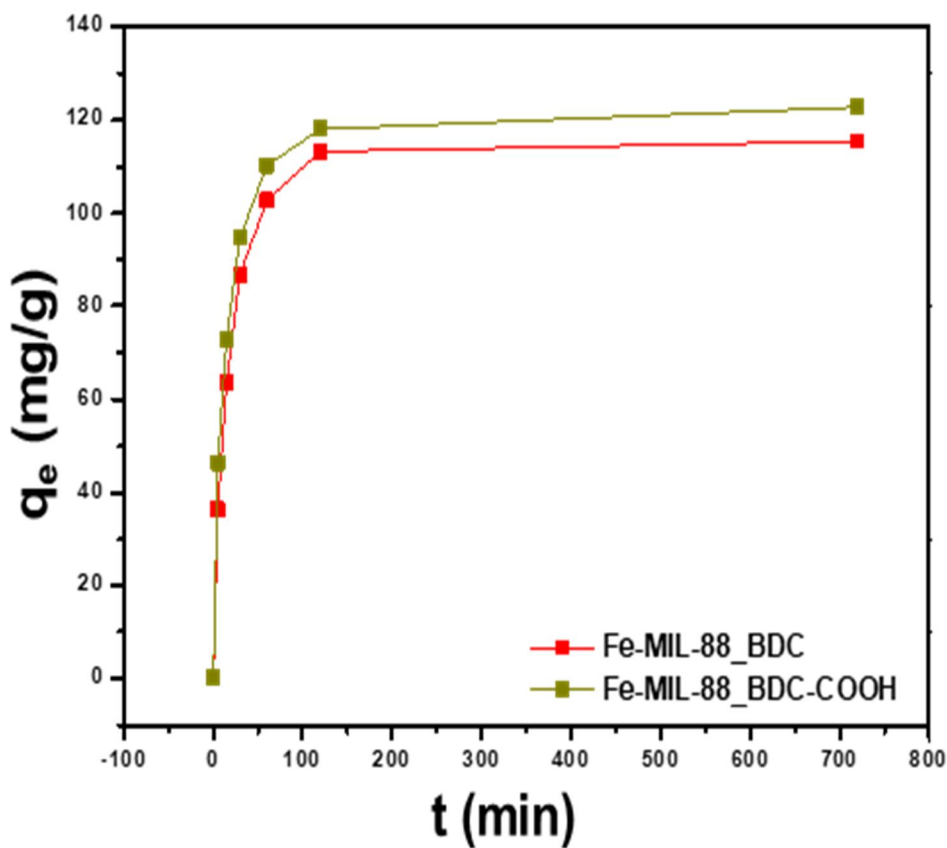


Figure 29. Adsorption kinetics of 3-MCPD uptakes in Fe-MIL-88_BDC

and Fe-MIL-88_BDC-COOH

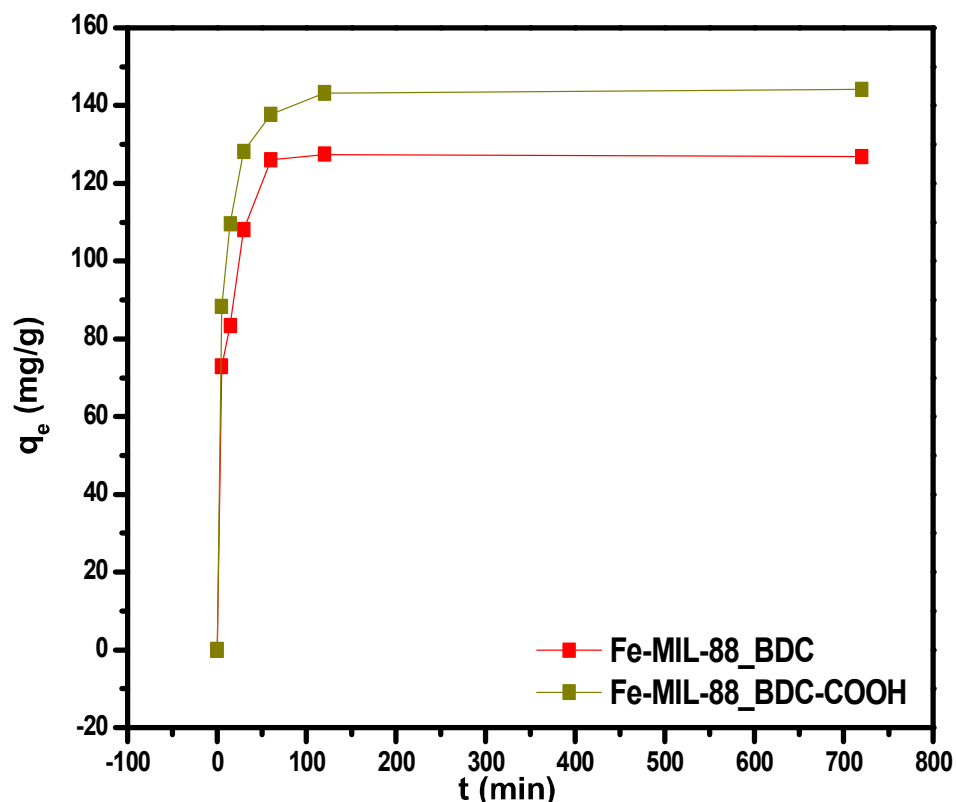


Figure 30. Adsorption kinetics of glycidol uptakes in Fe-MIL-88_BDC

and Fe-MIL-88_BDC-COOH

Table 13 Kinetic parameters of the pseudo-first order model and the pseudo-second order model for 3-MCPD and glycidol adsorption

3-MCPD	Pseudo-first order kinetic model			Pseudo-second order kinetic model		
	q _e	k ₁	R ²	q _e	k ₂	R ²
Fe-MIL-88_BDC	111.406	0.056	0.9846	121.060	0.0007	0.9954
Fe-MIL-88_BDC-COOH	116.263	0.070	0.9731	125.753	0.0008	0.9966
Glycidol	q _e	k ₁	R ²	q _e	k ₂	R ²
Fe-MIL-88_BDC	121.643	0.117	0.9214	129.398	0.0016	0.9703
Fe-MIL-88_BDC-COOH	136.019	0.174	0.9603	144.493	0.0019	0.9942

3.4.2. Adsorption isotherms

Figure 31 shows the adsorption isotherms of quinoline for Fe-MIL-88_BDC and Fe-MIL-88_BDC-COOH. The adsorption amounts of Fe-MIL-88_BDC is higher than those of Fe-MIL-88_BDC. To analyze the isotherms of quinoline adsorption, the experimental data were fitted to the Langmuir and Freundlich model. The isotherm parameters were listed in **Table 14**. All samples were better fitted to the Langmuir model than Freundlich model due to the value of correlation coefficient. This means that monolayer adsorption of quinoline occurs at homogenous sites. The value of Q_{max}^0 of Fe-MIL-88_BDC-COOH was higher than that of Fe-MIL-88_BDC. The reasons for the result are the high surface area and acid-base interactions between the carboxyl-functionalized ligand and quinoline. To verify the acid-base interaction by carboxyl-functionalization of the ligand, the adsorption isotherm was normalized. As shown in **Figure 32 and Table 15**, The value of Q_{max}^0 divided by the surface area is also higher for the Fe-MIL-88_BDC-COOH. This means that there is additional interaction which indicates an acid-base interaction between carboxyl-functionalized ligand and quinoline.

To evaluate the adsorption isotherms of 3-MCPD and glycidol, batch adsorption experiments were conducted at room temperature with different concentrations. **Figure 33 and Figure 34** shows the experimental data of

adsorption of 3-MCPD and glycidol. The parameters of the Langmuir and Freundlich model were listed in **Table 16**. In the cases of both 3-MCPD and glycidol, the value of correlation coefficient of Langmuir model was higher than the value of Freundlich model. Thus, Langmuir model were fitted better than Freundlich model for adsorption of 3-MCPD and glycidol. Comparing the value of Q_{max}^0 of Fe-MIL-88_BDC and Fe-MIL-88_BDC-COOH for adsorption of 3-MCPD and glycidol, adsorption amounts of Fe-MIL-88_BDC was higher than that of the Fe-MIL-88_BDC. The high surface area and covalent bond formation between carboxyl group of the ligand and two adsorbates are the main factors that make Fe-MIL-88_BDC-COOH adsorb the adsorbates more. Similar to adsorption of quinoline, the adsorption isotherm was normalized to determine the effect of covalent bonds with carboxyl group and adsorbates. As shown in **Figure 35, 36 and Table 17**, The value of Q_{max}^0 divided by the surface area is also higher for the Fe-MIL-88_BDC-COOH. Therefore, the adsorption isotherms revealed that the carboxyl-functionalized Fe-MIL-88 showed better adsorption performance than the unmodified Fe-MIL-88s. These results show that carboxyl-functionalized Fe-MIL-88_BDC is useful for removing toxic chemicals in oily phase.

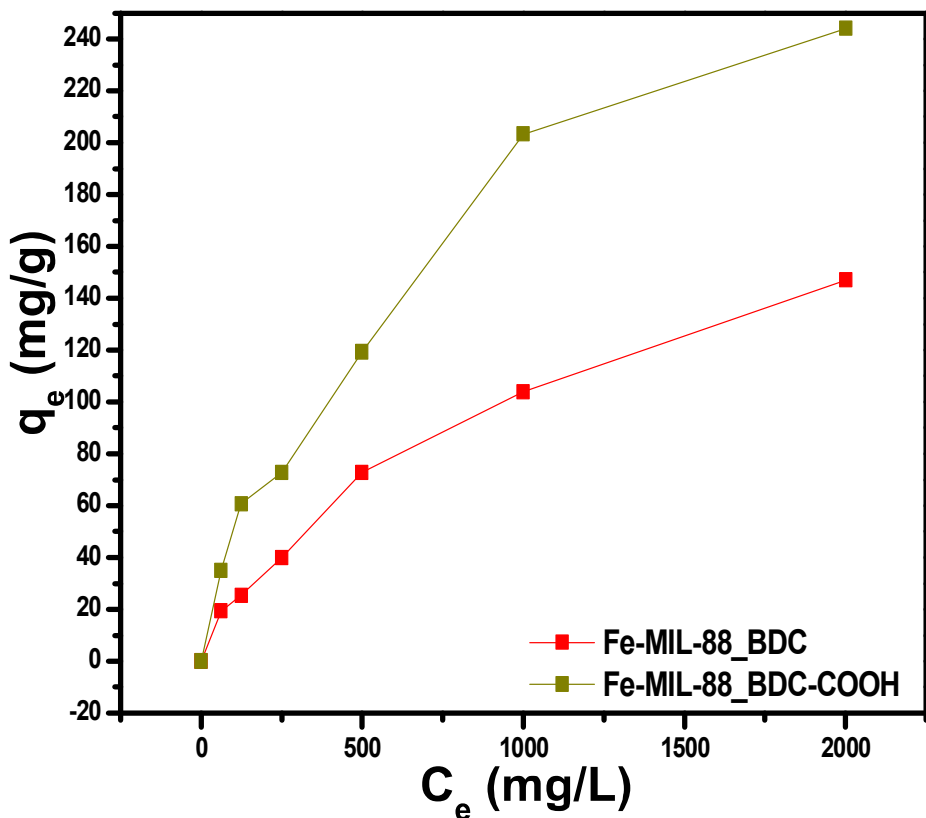


Figure 31. Adsorption isotherms of quinoline uptakes in Fe-MIL-88_BDC and Fe-MIL-88_BDC-COOH

Table 14. Isotherm parameters of the Freundlich model; (a) and Langmuir model; (b) for quinoline adsorption

Freundlich	K_f	n	R^2
Fe-MIL-88_BDC	1.7846	0.5830	0.9902
Fe-MIL-88_BDC-COOH	4.5324	0.5307	0.9640

(a)

Langmuir	Q_{max}^0	K_L	R^2
Fe-MIL-88_BDC	222.3	0.0009	0.9941
Fe-MIL-88_BDC-COOH	347.7	0.0012	0.9751

(b)

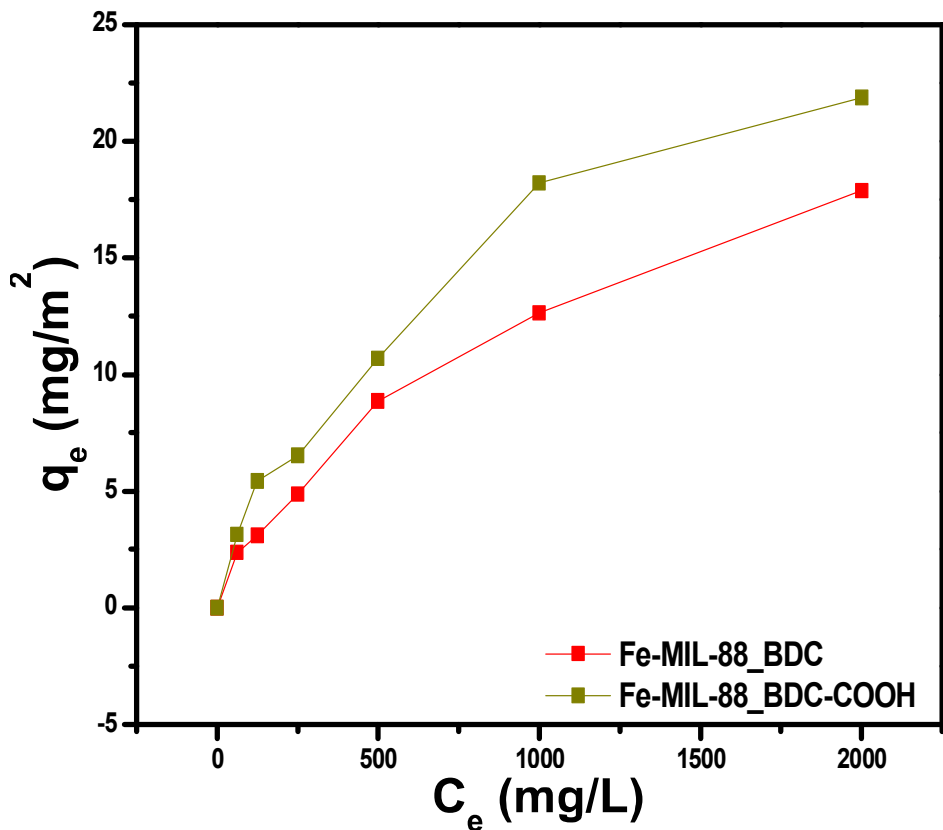


Figure 32. Normalizing of adsorption isotherms for quinoline uptakes in Fe-MIL-88_BDC and Fe-MIL-88_BDC-COOH

Table 15. Normalized isotherm parameters of the Freundlich model; (a) and Langmuir model; (b) for quinoline adsorption

Freundlich	K_f	n	R^2
Fe-MIL-88_BDC	0.2170	0.5830	0.9902
Fe-MIL-88_BDC-COOH	0.4061	0.5307	0.9640

(a)

Langmuir	Q_{max}^0	K_L	R^2
Fe-MIL-88_BDC	27.03	0.0009	0.9941
Fe-MIL-88_BDC-COOH	31.15	0.0012	0.9751

(b)

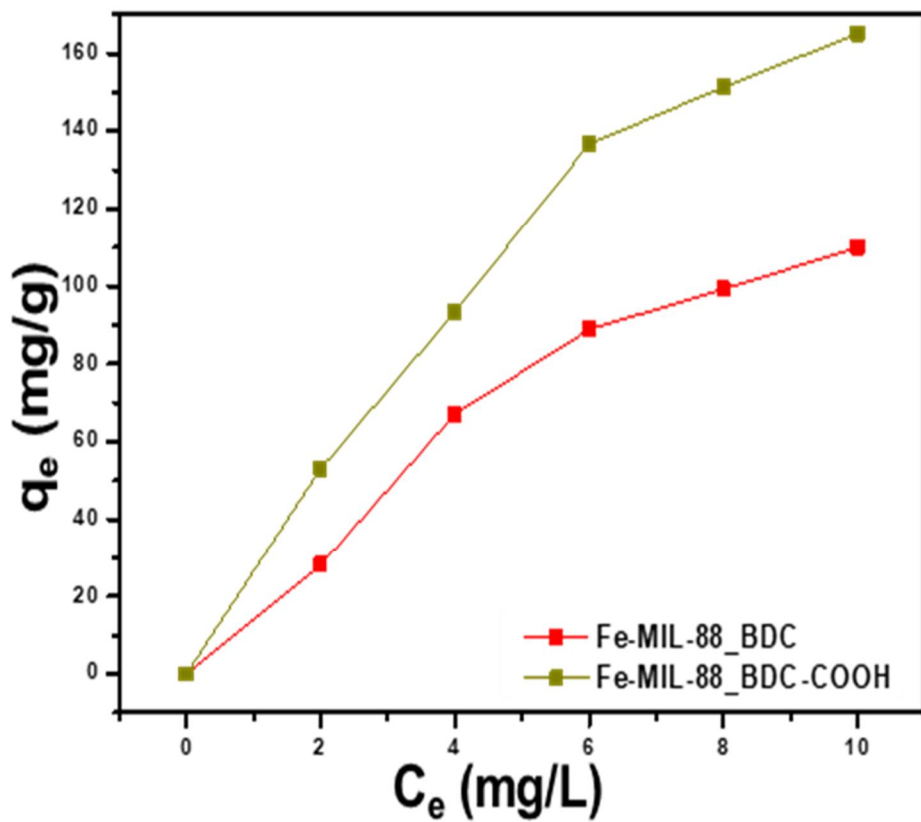


Figure 33. Adsorption isotherms of 3-MCPD uptakes in Fe-MIL-88_BDC and Fe-MIL-88_BDC-COOH

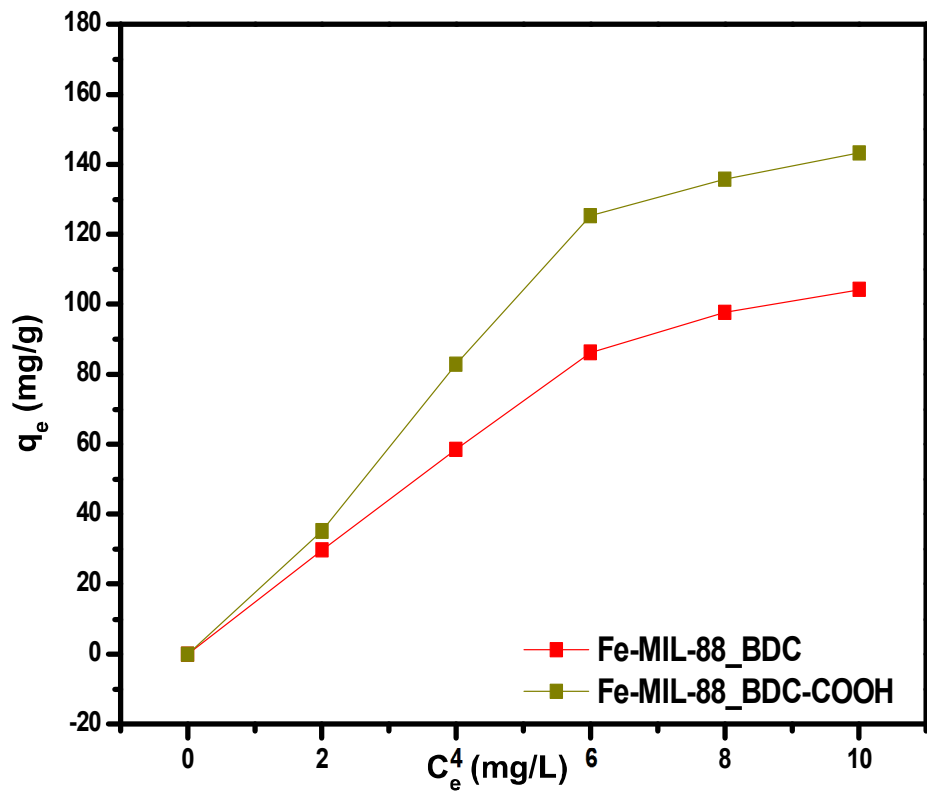


Figure 34. Adsorption isotherms of glycidol uptakes in Fe-MIL-88_BDC and Fe-MIL-88_BDC-COOH

Table 16. Isotherm parameters of the Freundlich model and Langmuir model for 3-MCPD and glycidol

3-MCPD	Freundlich isotherm model			Langmuir isotherm model		
	K _f	n	R ²	Q _{max} ^o	K _L	R ²
Fe-MIL-88_BDC	23.952	0.682	0.9302	233.969	0.093	0.9840
Fe-MIL-88_BDC-COOH	38.627	0.650	0.9548	333.508	0.103	0.9917
Glycidol	K _f	n	R ²	Q _{max} ^o	K _L	R ²
Fe-MIL-88_BDC	22.536	0.690	0.9422	232.791	0.087	0.9872
Fe-MIL-88_BDC-COOH	30.686	0.702	0.8919	327.273	0.086	0.9688
adsorption						

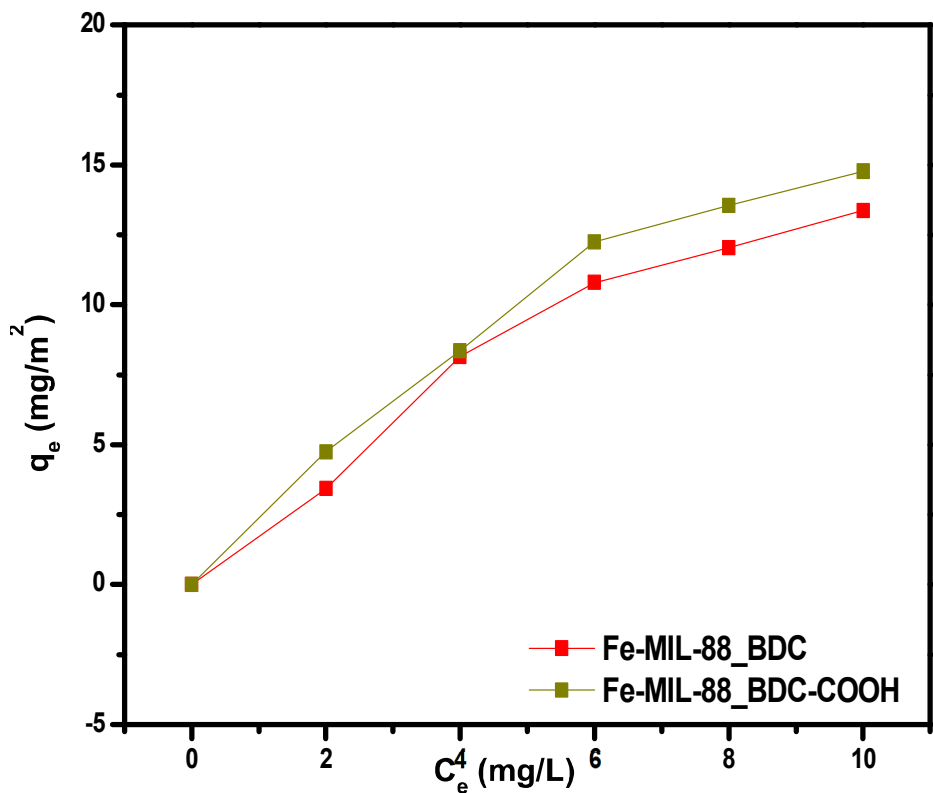


Figure 35. Normalized adsorption isotherms of 3-MCPD uptakes in Fe-MIL-88_BDC and Fe-MIL-88_BDC-COOH

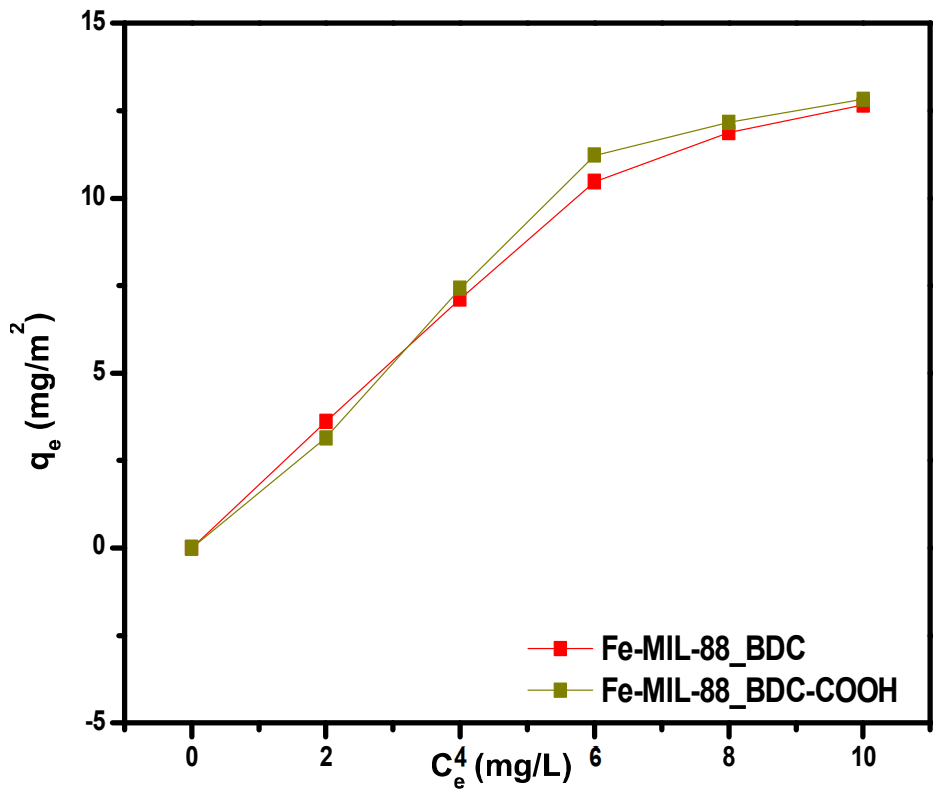


Figure 36. Normalized adsorption isotherms of glycidol uptakes in Fe-MIL-88_BDC and Fe-MIL-88_BDC-COOH

Table 17. Normalized isotherm parameters of the Freundlich model and Langmuir model for 3-MCPD and

3-MCPD	Freundlich isotherm model			Langmuir isotherm model		
	K_f	n	R²	Q_{max}^o	K_L	R²
Fe-MIL-88_BDC	2.913	0.682	0.9302	28.45	0.093	0.9840
Fe-MIL-88_BDC-COOH	3.461	0.650	0.9548	29.88	0.102	0.9917
Glycidol	K_f	n	R²	Q_{max}^o	K_L	R²
Fe-MIL-88_BDC	2.741	0.690	0.9422	28.31	0.087	0.9872
Fe-MIL-88_BDC-COOH	2.749	0.702	0.8919	29.32	0.086	0.9688

glycidol adsorption

4. Conclusion

In this research, we prepared various Metal-Organic Frameworks to remove toxic chemicals such as quinoline, 3-MCPD and glycidol in oily phase. Three types of MOFs were synthesized according to the types of ligands, and named as Fe-MIL-88_NDC, BDC, and BPDC, respectively. FT-IR, XRD, FE-SEM and HR-TEM analysis identified the successful synthesis of various Fe-MIL-88s. Among the three types of Fe-MIL-88s, the surface area and pore volume of Fe-MIL-88_BDC which was synthesized with terephthalic acid were the highest and the thermal stability was also the highest. This was verified through nitrogen adsorption-desorption and TGA analysis. In the case of quinoline, Fe-MIL-88_BDC showed the highest adsorption performance because of the high surface area, which increased the number of open metal sites that could form acid-base interactions with quinoline. Similarly, in 3-MCPD and glycidol, the adsorption performance of Fe-MIL-88_BDC was excellent due to the high surface area. Even in the kinetics, it was confirmed that the adsorption rate in Fe-MIL-88_BDC was the fastest for all toxic chemicals.

To further increase the adsorption performance of Fe-MIL-88_BDC, the organic ligands were functionalized with carboxylic acid. Nitrogen adsorption-desorption analysis showed the surface area and pore volume of

carboxyl-functionalized Fe-MIL-88_BDC were higher than that of conventional Fe-MIL-88_BDC. This is because pore contraction is interfered with the functionalization of the ligands. For all toxic chemicals, the maximum adsorption performance was higher due to the increased surface area and additional acid-base interaction and covalent bond with carboxyl-functionalization. Adsorption rates were also higher for carboxyl-functionalized Fe-MIL-88.

As a result, this study expected to provide the concepts of adsorption of toxic chemicals and fundamental understanding for improvement of removal capacity in oily phase with MOFs.

References

1. Ladshaw, A.P., et al., *Adsorbents and adsorption models for capture of Kr and Xe gas mixtures in fixed-bed columns*. Chemical Engineering Journal, 2019. **375**.
2. Ja'fari, M., S.L. Ebrahimi, and M.R. Khosravi-Nikou, *Ultrasound-assisted oxidative desulfurization and denitrogenation of liquid hydrocarbon fuels: A critical review*. Ultrason Sonochem, 2018. **40**(Pt A): p. 955-968.
3. Ahmed, I. and S.H. Jhung, *Remarkable adsorptive removal of nitrogen-containing compounds from a model fuel by a graphene oxide/MIL-101 composite through a combined effect of improved porosity and hydrogen bonding*. J Hazard Mater, 2016. **314**: p. 318-325.
4. Ahmed, I., N.A. Khan, and S.H. Jhung, *Adsorptive denitrogenation of model fuel by functionalized UiO-66 with acidic and basic moieties*. Chemical Engineering Journal, 2017. **321**: p. 40-47.
5. Gui, M.M., K.T. Lee, and S. Bhatia, *Feasibility of edible oil vs. non-edible oil vs. waste edible oil as biodiesel feedstock*. Energy, 2008. **33**(11): p. 1646-1653.
6. Prado, G.H.C., Y. Rao, and A. de Klerk, *Nitrogen Removal from Oil*:

- A Review*. Energy & Fuels, 2016. **31**(1): p. 14-36.
7. Rameshraja, D., et al., *Quinoline adsorption onto granular activated carbon and bagasse fly ash*. Chemical Engineering Journal, 2012. **181-182**: p. 343-351.
 8. Sarker, M., J.Y. Song, and S.H. Jhung, *Carboxylic-acid-functionalized UiO-66-NH₂: A promising adsorbent for both aqueous- and non-aqueous-phase adsorptions*. Chemical Engineering Journal, 2018. **331**: p. 124-131.
 9. Ahmed, I., et al., *Adsorptive denitrogenation of model fuels with porous metal-organic frameworks (MOFs): Effect of acidity and basicity of MOFs*. Applied Catalysis B: Environmental, 2013. **129**: p. 123-129.
 10. Sarker, M., et al., *Adsorptive removal of indole and quinoline from model fuel using adenine-grafted metal-organic frameworks*. J Hazard Mater, 2018. **344**: p. 593-601.
 11. Gibon, V., W. De Greyt, and M. Kellens, *Palm oil refining*. European Journal of Lipid Science and Technology, 2007. **109**(4): p. 315-335.
 12. Hrcicirik, K. and G. van Duijn, *An initial study on the formation of 3-MCPD esters during oil refining*. European Journal of Lipid Science and Technology, 2011. **113**(3): p. 374-379.
 13. Abraham, K., et al., *Relative oral bioavailability of 3-MCPD from 3-*

- MCPD fatty acid esters in rats.* Arch Toxicol, 2013. **87**(4): p. 649-59.
14. Ahmed, I. and S.H. Jhung, *Adsorptive desulfurization and denitrogenation using metal-organic frameworks.* J Hazard Mater, 2016. **301**: p. 259-76.
15. Katzer, J.R. and R. Sivasubramanian, *Process and Catalyst Needs for Hydrodenitrogenation.* Catalysis Reviews, 1979. **20**(2): p. 155-208.
16. Xie, L.L., et al., *Selective Adsorption of Neutral Nitrogen Compounds from Fuel Using Ion-Exchange Resins.* Journal of Chemical and Engineering Data, 2010. **55**(11): p. 4849-4853.
17. Hasan, Z., J. Jeon, and S.H. Jhung, *Oxidative desulfurization of benzothiophene and thiophene with WO_x/ZrO₂ catalysts: effect of calcination temperature of catalysts.* J Hazard Mater, 2012. **205-206**: p. 216-21.
18. Mguni, L.L., et al., *Ultra-deep desulphurization of both model and commercial diesel fuels by adsorption method.* Journal of Environmental Chemical Engineering, 2019. **7**(2).
19. Ahmed, I., et al., *Adsorptive denitrogenation of model fossil fuels with Lewis acid-loaded metal-organic frameworks (MOFs).* Chemical Engineering Journal, 2014. **255**: p. 623-629.
20. Ahmed, I., et al., *Adsorption of Nitrogen-Containing Compounds from Model Fuel over Sulfonated Metal-Organic Framework:*

- Contribution of Hydrogen-Bonding and Acid–Base Interactions in Adsorption.* The Journal of Physical Chemistry C, 2015. **120**(1): p. 407-415.
21. Furukawa, H., et al., *The chemistry and applications of metal-organic frameworks*. Science, 2013. **341**(6149): p. 1230444.
 22. Yuan, S., et al., *Stable Metal-Organic Frameworks: Design, Synthesis, and Applications*. Adv Mater, 2018. **30**(37): p. e1704303.
 23. Van de Voorde, B., et al., *Adsorptive separation on metal-organic frameworks in the liquid phase*. Chem Soc Rev, 2014. **43**(16): p. 5766-88.
 24. Van de Voorde, B., et al., *N/S-heterocyclic contaminant removal from fuels by the mesoporous metal-organic framework MIL-100: the role of the metal ion*. J Am Chem Soc, 2013. **135**(26): p. 9849-56.
 25. Vellingiri, K., et al., *Metal-organic frameworks for the adsorption of gaseous toluene under ambient temperature and pressure*. Chemical Engineering Journal, 2017. **307**: p. 1116-1126.
 26. Andrew Lin, K.-Y. and Y.-T. Hsieh, *Copper-based metal organic framework (MOF), HKUST-1, as an efficient adsorbent to remove p-nitrophenol from water*. Journal of the Taiwan Institute of Chemical Engineers, 2015. **50**: p. 223-228.
 27. Xuan Huynh, N.T., V. Chihaiia, and D.N. Son, *Hydrogen storage in*

- MIL-88 series.* Journal of Materials Science, 2018. **54**(5): p. 3994-4010.
28. Mellot-Draznieks, C., *Role of computer simulations in structure prediction and structure determination: from molecular compounds to hybrid frameworks.* Journal of Materials Chemistry, 2007. **17**(41).
 29. Surble, S., et al., *A new isoreticular class of metal-organic-frameworks with the MIL-88 topology.* Chem Commun (Camb), 2006(3): p. 284-6.
 30. Qian, Y., et al., *Fe/Fe₃C/N-Doped Carbon Materials from Metal-Organic Framework Composites as Highly Efficient Oxygen Reduction Reaction Electrocatalysts.* ChemPlusChem, 2016. **81**(8): p. 718-723.
 31. Gholizadeh Khasevani, S., N. Mohaghegh, and M.R. Gholami, *Kinetic study of navy blue photocatalytic degradation over Ag₃PO₄/BiPO₄@MIL-88B(Fe)@g-C₃N₄ core@shell nanocomposite under visible light irradiation.* New Journal of Chemistry, 2017. **41**(18): p. 10390-10396.
 32. Bara, D., et al., *Kinetic Control of Interpenetration in Fe-Biphenyl-4,4'-dicarboxylate Metal-Organic Frameworks by Coordination and Oxidation Modulation.* J Am Chem Soc, 2019. **141**(20): p. 8346-8357.
 33. Li, X., et al., *Facilitation of the visible light-induced Fenton-like*

- excitation of H₂O₂ via heterojunction of g-C₃N₄/NH₂-Iron terephthalate metal-organic framework for MB degradation.* Applied Catalysis B: Environmental, 2017. **202**: p. 653-663.
34. Ko, N., et al., *Tailoring the water adsorption properties of MIL-101 metal-organic frameworks by partial functionalization.* Journal of Materials Chemistry A, 2015. **3**(5): p. 2057-2064.
35. Lee, J.H. and S.-Y. Kwak, *Rapid adsorption of bisphenol A from wastewater by β-cyclodextrin-functionalized mesoporous magnetic clusters.* Applied Surface Science, 2019. **467-468**: p. 178-184.
36. Lin, C., et al., *Rice husk grafted PMAA by ATRP in aqueous phase and its adsorption for Ce 3+.* Chemical Physics Letters, 2017. **690**: p. 68-73.
37. Tran, H.N., et al., *Mistakes and inconsistencies regarding adsorption of contaminants from aqueous solutions: A critical review.* Water Res, 2017. **120**: p. 88-116.
38. Serre, C., et al., *Role of solvent-host interactions that lead to very large swelling of hybrid frameworks.* Science, 2007. **315**(5820): p. 1828-1831.
39. Scherb, C., A. Schodel, and T. Bein, *Directing the structure of metal-organic frameworks by oriented surface growth on an organic monolayer.* Angew Chem Int Ed Engl, 2008. **47**(31): p. 5777-9.

40. Deng, H.X., et al., *Large-Pore Apertures in a Series of Metal-Organic Frameworks*. Science, 2012. **336**(6084): p. 1018-1023.
41. Wang, J., et al., *Metal-organic frameworks MIL-88A with suitable synthesis conditions and optimal dosage for effective catalytic degradation of Orange G through persulfate activation*. RSC Advances, 2016. **6**(113): p. 112502-112511.
42. Horcajada, P., et al., *How linker's modification controls swelling properties of highly flexible iron(III) dicarboxylates MIL-88*. J Am Chem Soc, 2011. **133**(44): p. 17839-47.
43. Ramsahye, N.A., et al., *Impact of the Flexible Character of MIL-88 Iron(III) Dicarboxylates on the Adsorption of n-Alkanes*. Chemistry of Materials, 2013. **25**(3): p. 479-488.
44. Nguyen, L.T.L., et al., *Towards applications of metal-organic frameworks in catalysis: Friedel-Crafts acylation reaction over IRMOF-8 as an efficient heterogeneous catalyst*. Journal of Molecular Catalysis A: Chemical, 2011. **349**(1-2): p. 28-35.
45. Xie, D., et al., *Bifunctional NH₂-MIL-88(Fe) metal-organic framework nanoctahedra for highly sensitive detection and efficient removal of arsenate in aqueous media*. Journal of Materials Chemistry A, 2017. **5**(45): p. 23794-23804.
46. Mohr, S., et al., *Coverage-Dependent Anchoring of 4,4'-Biphenyl*

- Dicarboxylic Acid to CoO(111) Thin Films.* Langmuir, 2017. **33**(17): p. 4178-4188.
47. Pham, M.H., et al., *Novel route to size-controlled Fe-MIL-88B-NH₂ metal-organic framework nanocrystals.* Langmuir, 2011. **27**(24): p. 15261-7.
48. Zhou, F., et al., *Facile synthesis of MOFs with uncoordinated carboxyl groups for selective CO₂ capture via postsynthetic covalent modification.* RSC Advances, 2017. **7**(7): p. 3713-3719.
49. Gotthardt, M.A., et al., *Post-synthetic immobilization of palladium complexes on metal-organic frameworks – a new concept for the design of heterogeneous catalysts for Heck reactions.* RSC Advances, 2013. **3**(27).
50. McKinlay, A.C., et al., *Nitric Oxide Adsorption and Delivery in Flexible MIL-88(Fe) Metal–Organic Frameworks.* Chemistry of Materials, 2013. **25**(9): p. 1592-1599.
51. Raupp, Y.S., et al., *Aerobic oxidation of α -pinene catalyzed by homogeneous and MOF-based Mn catalysts.* Applied Catalysis A: General, 2017. **546**: p. 1-6.
52. Kim, S.N., et al., *Metal-organic frameworks, NH₂-MIL-88(Fe), as carriers for ophthalmic delivery of brimonidine.* Acta Biomater, 2018. **79**: p. 344-353.

53. Han, Y., et al., *Facile synthesis of morphology and size-controlled zirconium metal-organic framework UiO-66: the role of hydrofluoric acid in crystallization*. CrystEngComm, 2015. **17**(33): p. 6434-6440.
54. Meng, W., et al., *Porous Fe₃O₄/carbon composite electrode material prepared from metal-organic framework template and effect of temperature on its capacitance*. Nano Energy, 2014. **8**: p. 133-140.

국문 초록

퀴놀린, 3-MCPD, glycidyl ester와 같은 유중에 존재하는 여러 유해물질들은 인체와 환경에 악영향을 미친다고 알려져 있다. 유해물질을 제거하는 여러 방법들 중에서 흡착은 간단하며 가격경쟁력이 뛰어나며 재생성이 뛰어나다는 장점을 가지고 있다. 다양한 흡착제 중 Metal–Organic Frameworks (MOFs)는 기공의 구조를 조절하는데 용이하고 다양한 기능기를 도입할 수 있다는 특징 때문에 많은 주목을 받고 있는 흡착 소재이다. 다양한 MOF들 중에서 Fe–MIL–88은 가격이 저렴하고, 높은 화학적, 열적 안정성을 가지며 생체적합하고 기능화가 용이하다는 장점을 가지고 있다. 또한 다양한 리간드를 사용하여도 형상이 변하지 않는다는 특징을 가지고 있다. 이러한 장점 및 특징들에도 불구하고 유중에 적용된 사례가 없었다. 따라서 Fe–MIL–88을 유중 흡착에 적용함으로써 리간드의 종류와 기능화에 따라 흡착 성능이 어떻게 달라지는지에 관해 연구를 진행하였다. 합성된 Fe–MIL–88은 각각 Fe–MIL–88_NDC, BDC 그리고 BPDC로 명명하였고, 흡착 kinetic과 흡착 isotherm 분석을 통해 흡착속도와 최대 흡착량을 비교하였고, Fe–MIL–88_BDC가 속도론적인 측면에서나 최대흡착량에서나 가장

유중에 적합한 흡착소재임을 확인하였다. Fe-MIL-88_BDC에 카르복실기를 도입함으로써 기존의 Fe-MIL-88_BDC와의 흡착 성능을 비교하였고, 카르복실기를 도입한 Fe-MIL-88_BDC가 흡착 속도로나 최대흡착량으로나 성능이 개선됨을 확인하였다. 이는 높은 비표면적과 카르복실기와 리간드 사이의 추가적인 상호작용때문임을 흡착거동 분석을 통해 확인하였다. 본 연구의 결과는 카르복실기로 개질된 Fe-MIL-88_BDC는 유중에 존재하는 유해물질들을 제거하는데 탁월한 흡착소재임을 확인할 수 있었다.

감사의 글

길면서도 짧았던 2년간의 석사과정을 돌이켜보면서 그동안 저에게 많은 배움을 주었던 모든 분들께 정말 감사드립니다. 먼저 석사과정 동안 묵묵히 응원해주시고 언제나 베풀목이 되어주신 부모님께 깊은 감사를 드립니다.

2년의 학위 기간 동안 연구와 관련되어 끊임없이 지도해주시고 아낌없이 격려해주신 과승엽 교수님께 진심으로 감사드립니다. 또한 바쁘신 와중에 학위 심사를 해주시고 여러 조언을 해주신 박찬 교수님과 안철희 교수님께도 감사의 마음을 전하고 싶습니다.

모든 연구실 구성원 덕분에 너무나 부족하였던 제가 2년의 기간을 거쳐 무사히 졸업까지 할 수 있었던 것 같습니다. 먼저 저의 사수이시고 저의 연구주제를 같이 봐주시고 뒤에서 항상 저를 응원해주셨던 용준이형, 연구적으로나 생활적으로나 너무나 많은 도움을 주신 지환이형, 항상 진지하게 저의 연구에 관심 가져주시고 아낌없이 조언 해주셨던 태선이형, 같이 새벽까지 연구실에 있으면서 정말 많은 대화를 나누고 항상 격려 해주셨던 우진이형, 무슨 일이든 열심히 하고 도와주셨던 대연이형, 항상 동기로서 고생 많이 했던 왕우, 연구적으로 정말 많이 조언해주셨던 준형이형, 같이 많은 대화를 나누면서 위로와 격려 많이 해주셨던 병갑이형, 항상 긍정의 에너지를 주셨던 효빈이형에게 진심으로 감사드립니다.

지난 2년동안의 석사과정에서 배웠던 지식과 경험을 바탕으로 사회에서도 성실한 삶으로 나아가 보탬이 될 수 있는 사람이 되겠습니다. 진심으로 감사드립니다.